AGU PUBLICATIONS

JGR

Journal of Geophysical Research: Atmospheres

RESEARCH ARTICLE
10.1002/2013JD021186

Key Points:
- A fully explicit SOA formation model is used to determine SOA radiative forcing
- The direct radiative forcing by brown carbon in SOA is estimated
- The radiative forcing of OA in snow/ice is estimated for the first time

Correspondence to:
G. Lin,
gxlin@umich.edu

Citation:
Lin, G., J. E. Penner, M. G. Flanner, S. Sillman, L. Xu, and C. Zhou (2014), Radiative forcing of organic aerosol in the atmosphere and on snow: Effects of SOA and brown carbon, *J. Geophys. Res. Atmos.*, *119*, 7453–7476, doi:10.1002/2013JD021186.

Received 12 NOV 2013
Accepted 13 MAY 2014
Accepted article online 16 MAY 2014
Published online 18 JUN 2014

Radiative forcing of organic aerosol in the atmosphere and on snow: Effects of SOA and brown carbon

Guangxing Lin[1], Joyce E. Penner[1], Mark G. Flanner[1], Sanford Sillman[1], Li Xu[2], and Cheng Zhou[1]

[1]Department of Atmospheric, Oceanic, and Space Sciences, University of Michigan, Ann Arbor, Michigan, USA, [2]Scripps Institution of Oceanography, University of California, San Diego, California, USA

Abstract Organic aerosols (OA) play an important role in climate change. However, very few calculations of global OA radiative forcing include secondary organic aerosol (SOA) or the light-absorbing part of OA (brown carbon). Here we use a global model to assess the radiative forcing associated with the change in primary organic aerosol (POA) and SOA between present-day and preindustrial conditions in both the atmosphere and the land snow/sea ice. Anthropogenic emissions are shown to substantially influence the SOA formation rate, causing it to increase by 29 Tg/yr (93%) since preindustrial times. We examine the effects of varying the refractive indices, size distributions for POA and SOA, and brown carbon fraction in SOA. The increase of SOA exerts a direct forcing ranging from −0.12 to −0.31 W m^{-2} and a first indirect forcing in warm-phase clouds ranging from −0.22 to −0.29 W m^{-2}, with the range due to different assumed SOA size distributions and refractive indices. The increase of POA since preindustrial times causes a direct forcing varying from −0.06 to −0.11 W m^{-2}, when strongly and weakly absorbing refractive indices for brown carbon are used. The change in the total OA exerts a direct forcing ranging from −0.14 to −0.40 W m^{-2}. The atmospheric absorption from brown carbon ranges from +0.22 to +0.57 W m^{-2}, which corresponds to 27%~70% of the black carbon (BC) absorption predicted in the model. The radiative forcing of OA deposited in land snow and sea ice ranges from +0.0011 to +0.0031 W m^{-2} or as large as 24% of the forcing caused by BC in snow and ice simulated by the model.

1. Introduction

Organic aerosols (OA) make up a large fraction of submicron particulate mass in the troposphere [*Zhang et al.*, 2007]. Secondary organic aerosol (SOA) has been shown to contribute over 60% of the total OA mass in some environments [*Jimenez et al.*, 2009]. Even though these aerosols are thought to be formed primarily from biogenic emissions [*Hallquist et al.*, 2009; *Lin et al.*, 2012], their formation rates can increase as a result of changes in gas-phase oxidation rates, and therefore, they can enhance the direct and indirect climate forcings by aerosols. The change in the formation rates for the present-day (PD) versus preindustrial (PI) conditions was first highlighted by *Kanakidou et al.* [2000], but the forcing associated with the increases in SOA was not included in the International Panel on Climate Change (IPCC) reports until very recently [*International Panel on Climate Change* (*IPCC*), 2013], and very few global model estimates of this forcing exist. *Hoyle et al.* [2009] studied the change in SOA between PD and PI using an off-line chemistry transport model (Oslo CTM2) and estimated that this change could cause a total direct radiative forcing of −0.09 W/m^2. However, this study used a simple parameterization scheme (a two-product model) to simulate SOA formation. This scheme cannot account for certain complexities in the SOA formation system [*Hallquist et al.*, 2009; *Lin et al.*, 2012] and might not, for example, accurately predict the change in SOA due to the change in NO_x since PI times. Here we use a global model with an explicit calculation of the change in SOA between PD and PI conditions to estimate the forcing by SOA as well as by total OA.

OA particles are important not only for their scattering of visible radiation (which leads to cooling) but also because they may absorb light, which leads to warming. This light-absorbing OA component, also known as brown carbon (BrC), has been widely observed: during biomass burning [e.g., *Kirchstetter et al.*, 2004; *Marley et al.*, 2009; *Chen and Bond*, 2010; *Hecobian et al.*, 2010; *Lack et al.*, 2012; *Saleh et al.*, 2013], during coal burning [e.g., *Bond et al.*, 1999; *Bond*, 2001; *Yang et al.*, 2009; *Arola et al.*, 2011], in pollution outflow [e.g., *Kirillova et al.*, 2014], and during SOA formation [e.g., *Limbeck et al.*, 2003; *Hoffer et al.*, 2006; *Zhang et al.*, 2011,

2013; *Updyke et al.*, 2012; *Nakayama et al.*, 2013; *Lambe et al.*, 2013; *Liu et al.*, 2014]. These papers show that the contribution of BrC to the absorption by ultraviolet/visible light can be significant. *Bahadur et al.* [2012], using aerosol optical properties derived from AERONET (Aerosol Robotic Network) measurements, estimated that BrC absorption at 440 nm could be about 40% of the absorption by black carbon (BC) in California. Near Xianghe, China, BrC absorption was shown to explain around 30% of the total aerosol absorption at 370 nm, although this fraction decreased to about 10% at 550 nm [*Yang et al.*, 2009]. *Chung et al.* [2012] estimated that BrC could contribute 20% of the global average absorption by carbonaceous aerosols at 550 nm, if constrained by AERONET observations. *Feng et al.* [2013] used a global chemical transport model to calculate the absorption by BrC in biomass and biofuel-burning primary organic aerosols (POAs). They found that the contribution of BrC to the total atmospheric absorption could be as high as 19%. Despite the importance of BrC, most existing models usually assume the OA to be almost purely scattering, neglecting the light-absorbing properties of BrC.

Absorption by light-absorbing particles can be enhanced when these particles are deposited on land snow and sea ice. This can reduce the albedo of the snow because of its extremely high reflectivity, causing even larger short-wave absorption and warming. Black carbon, for example, is known to be an effective agent to reduce snow albedos and has been estimated to increase the global average absorption of the short-wave radiation in snow on land and sea ice by 0.01 W/m^2 to 0.09 W/m^2 [*Bond et al.*, 2013]. Using the measurements of hundreds of snow samples, *Doherty et al.* [2010] concluded that about 40% of the light absorption from impurities in Arctic snow and sea ice is due to non-BC constituents. However, no global models have estimated the role of BrC in the reduction of snow albedo.

In the present study, we employ a 3-D chemical transport model (CTM) with an explicit SOA formation mechanism to calculate the change in the production and burden of POA and SOA between the PD and PI conditions. We note that there are still gaps in our understanding of the formation mechanisms for SOA production [*Spracklen et al.*, 2011]; however, the current model is able to reproduce observations reasonably well [*Lin et al.*, 2012, 2014]. We use an off-line radiative transfer model to evaluate the radiative forcing caused by the change in POA and SOA since PI times. We also make some simplifying assumptions to understand the importance of BrC absorption in the amount of radiation absorbed within the atmospheric column. Finally, we use two 3-D models (a land model and a sea-ice model) to estimate the radiative forcing due to the organic aerosol deposited in land snow and sea ice.

2. Model Description

2.1. IMPACT Model

We used the Integrated Massively Parallel Atmospheric Chemical Transport (IMPACT) model run at a 4° latitude × 5° longitude horizontal resolution with 46 vertical layers to predict the POA and SOA concentrations in the atmosphere as well as their deposition rates on snow and ice. The model includes the microphysics of sulfate aerosol including the formation of internal mixtures of sulfate and nonsulfate aerosols [*Liu et al.*, 2005; *Lin et al.*, 2012] and was run using the 1997 meteorological fields from the NASA Data Assimilation Office GEOS–Stratospheric Tracers of Atmospheric Transport model [*Coy and Swinbank*, 1997]. The same meteorological data were used for both the present-day and preindustrial simulations.

The SOA module used in IMPACT accounts for the formation of SOA from organic nitrates and peroxides, dicarbonyls, and epoxides [*Lin et al.*, 2012]. We employ traditional gas-particle partitioning to treat the formation of SOA from organic nitrates and peroxides, which are predicted using an explicit full chemistry scheme. This includes the HO_x recycling mechanism proposed by *Peeters et al.* [2009] but with a reduced rate for the 1,5-H and 1,6-H shifts in isoprene radicals by a factor of 10 [*Lin et al.*, 2012, scheme "C"]. The condensed semivolatile organic compounds (SVOCs) that form from gas-particle partitioning are assumed to undergo further aerosol-phase reactions to form oligomers with a 1 day *e*-folding lifetime. We also include the aqueous-phase formation of SOA from glyoxal and methylglyoxal, using a full aqueous-phase chemistry scheme that mainly follows *Lim et al.* [2005], *Deguillaume et al.* [2010], and *Waxman et al.* [2013] [*Lin et al.*, 2014, Case 5]. The formation of gas-phase epoxides from isoprene oxidation following *Paulot et al.* [2009] is also included together with their aerosol formation on aqueous sulfate aerosol following *Fu et al.* [2008]. A full description and a validation of the original SOA scheme against measurements is given by *Lin et al.* [2012], while *Lin et al.* [2014] update the comparisons using the aqueous formation scheme. The model is able to

Table 1. Global Emissions of Gases, Aerosols, and Aerosol Precursors

Species	PD (≈2000)	PI (≈1870)	Reference
SO_2			
Fossil fuel and industry	61.3 Tg S/yr	1.5 Tg S/yr	*Smith et al.* [2001]
Volcanoes	4.8 Tg S/yr	4.8 Tg S/yr	*Andres and Kasgnoc* [1998]
DMS	26.1 Tg S/yr	26.1 Tg S/yr	*Kettle and Andreae* [2000]
NO			
Fossil fuel	22.7 Tg N/yr	1.0 Tg N/yr	*Van Aardenne et al.* [2001]
Biomass burning	9.3 Tg N/yr	4.8 Tg N/yr	*Ito et al.* [2007]
Soil	5.5 Tg N/yr	2.9 Tg N/yr	*Van Aardenne et al.* [2001]
Lighting	3.0 Tg N/yr	3.0 Tg N/yr	*Ito et al.* [2007]
Aircraft	0.9 Tg N/yr	0	*Ito et al.* [2007]
Ship	0.7 Tg N/yr	0	*Ito et al.* [2007]
CO	426.0 Tg C/yr	126 Tg C/yr	*Ito et al.* [2007]
Methyl ethyl ketone(>C3 ketones)	5.8 Tg C/yr	0	*Ito et al.* [2007]
C_2H_6	9.3 Tg C/yr	0	*Ito et al.* [2007]
C_3H_8	7.3 Tg C/yr	0	*Ito et al.* [2007]
ALK4(>=C4 alkanes)	15.3 Tg C/yr	0	*Ito et al.* [2007]
Acetaldehyde	3.3 Tg C/yr	0	*Ito et al.* [2007]
CH_2O	2.4 Tg C/yr	0	*Ito et al.* [2007]
ALK7(C6–C8 alkanes)	11.3 Tg C/yr	0	*Ito et al.* [2007]
Benzene	3.2 Tg C/yr	0	*Ito et al.* [2007]
Toluene	5.8 Tg C/yr	0	*Ito et al.* [2007]
Xylene	3.9 Tg C/yr	0	*Ito et al.* [2007]
Trans-2-butene	6.6 Tg C/yr	0	*Ito et al.* [2007]
HCOOH	2.6 Tg C/yr	0	*Ito et al.* [2007]
Acetic acid	12.4 Tg C/yr	0	*Ito et al.* [2007]
Phenol	4.3 Tg C/yr	0	*Ito et al.* [2007]
Ocean source of POA	34.5 Tg OM/yr	34.5 Tg OM/yr	*O'Dowd et al.* [2008]
DMS source of MSA	8.2 Tg/yr	8.2 Tg/yr	*Gondwe et al.* [2003]
Fossil fuel + biofuel POA	15.7 Tg OM/yr	5.1 Tg OM/yr	*Ito and Penner* [2005] and *Wang et al.* [2009]
Fossil fuel + biofuel BC	5.8 Tg BC/yr	0.8 Tg BC/yr	*Ito and Penner* [2005] and *Wang et al.* [2009]
Biomass-burning OA	47.4 Tg OM/yr	17.9 Tg OM/yr	*Ito and Penner* [2005]
Biomass-burning BC	4.7 Tg BC/yr	1.8 Tg BC/yr	*Ito and Penner* [2005]
Isoprene	472.0 Tg C/yr	472.0 Tg C/yr	*Guenther et al.* [1995]
α-pinene	78.8 Tg C/yr	78.8 Tg/yr	*Guenther et al.* [1995] and *Wang et al.* [2009]
Limonene	38.8 Tg C/yr	38.8 Tg C/yr	*Guenther et al.* [1995] and *Wang et al.* [2009]
Propene	24.2 Tg C/yr	12.9 Tg C/yr	*Ito et al.* [2007]
Methanol	42.9 Tg C/yr	33.4 Tg C/yr	*Ito et al.* [2007]
Acetone	44.5 Tg C/yr	20.2 Tg C/yr	*Ito et al.* [2007]
Ethene	28.2 Tg C/yr	10.3 Tg C/yr	*Ito et al.* [2007]

capture the observed SOA reasonably well in both the northern hemisphere and the tropical regions with a normalized mean bias of −33.2% and +19.3%, respectively [*Lin et al.*, 2014].

We assume a standard set of anthropogenic emissions that are close to the emissions for 2000 for the PD and close to 1870 for PI conditions, except as noted below (Table 1). Biogenic emissions are a function of temperature and CO_2 concentrations but were held constant for these estimates. Terrestrial isoprene emissions are based on a modified version of the inventory of *Guenther et al.* [1995] [*Wang et al.*, 1998; *Bey et al.*, 2001] and have a total source strength of 470.8 Tg C/yr. The total marine isoprene emissions, 0.9 Tg C/yr, are from the estimate by *Gantt et al.* [2009] based on satellite observations. The biogenic terpene source was 117.6 Tg C/yr and is based on the work of *Guenther et al.* [1995] as modified by *Wang et al.* [1998]. The other temperature-dependent biogenic VOC emissions for ethane, propene, acetone, and methanol are distributed according to the emissions of isoprene following *Ito et al.* [2007]. Methane mixing ratios for PD and PI conditions were set to 1770 ppb and 800 ppb, similar to the measurements summarized by *Forster et al.* [2007]. For the PI experiments, all fossil fuel related and industrial emissions of VOCs are set to zero. The primary sea spray organic source was estimated using the correlation between chlorophyll *a* and the fractional water insoluble organic mass of sea salt, following *O'Dowd et al.* [2008], where the chlorophyll-*a* concentrations were those measured by the Moderate Resolution Imaging Spectroradiometer Aqua

instrument averaged for the 4 years from 2004 to 2008. Anthropogenic and natural sulfur emissions for PD and PI were those specified by *Wang and Penner* [2009]. In particular, anthropogenic sulfur emissions were developed based on the emission data of *Smith et al.* [2001], volcanic SO_2 emissions were from the work of *Andres and Kasgnoc* [1998], and marine dimethyl sulfide (DMS) fluxes were based on the estimates from *Kettle and Andreae* [2000]. The anthropogenic NO_x emissions from fossil fuel combustion and soil emissions were adopted from *van Aardenne et al.* [2001] for 1990, while those from biomass burning and lightning were based on the work of *Ito et al.* [2007] for 1990. Fossil fuel and biofuel emissions of organic matter (OM) and BC were those estimated by *Ito and Penner* [2005] but with the fossil fuel emissions adjusted by *Wang et al.* [2009] to better fit surface observations. Open biomass-burning BC and OM emissions were developed using *Ito and Penner*'s [2005] emissions for BC as an a priori estimate together with the inverse model approach of *Zhang et al.* [2005]. The treatments of dry and wet deposition used here for both gas- and aerosol-phase species are the same as those used by *Lin et al.* [2012].

2.2. Radiative Transfer Model

We use an off-line radiative transfer model to calculate the optical properties of aerosols and their resulting radiative forcing [*Penner et al.*, 2011a; *Wang and Penner*, 2009]. The forcing associated with OA was calculated from the difference in the radiation flux with all the PD concentrations and that calculated assuming that all the aerosols had their PD concentrations except those for OA, which was specified at their PI concentrations.

We used monthly average aerosol concentrations together with four-hourly meteorological fields to estimate instantaneously varying aerosol optical depths, which vary with water uptake by the aerosols. Four-hourly aerosol optical depth is calculated using a look-up table that included the optical properties as a function of wavelength and size parameter, so that arbitrary internal mixtures and sizes can be included. Five types of aerosol populations are assumed to be externally mixed (i.e., pure sulfate, fossil fuel OA/BC, biomass-burning OA/BC, dust, and sea salt), but each nonsulfate aerosol type includes the calculated amount of sulfate coating. In the model, sulfate can "coat" nonsulfate aerosols as a result of the condensation of sulfuric acid, by coagulation with pure sulfate aerosols, and by the aqueous formation of sulfate. This coated sulfate is assumed to be internally mixed with nonsulfate aerosols. SOA is either added to the fossil fuel OA field or to the biomass-burning OA field, depending on which size distribution for these compounds is assumed (see Table 4). The refractive index for internally mixed aerosols (including mixing with water which is treated using the Köhler equation) is calculated based on the weighted volume mixture for each aerosol type. The refractive indices at 550 nm are $1.53-10^{-7}$ i for sulfate, $1.53-1.4\times10^{-3}$ i for dust, and $1.38-5.8\times10^{-7}$ for sea salt, which follow choices made by *Liu et al.* [2007], while that for black carbon, 1.85–0.71 i, is from *Bond and Bergstrom* [2006]. As noted above, the off-line radiative transfer model uses monthly average aerosol concentrations, but the uptake of water with relative humidity and resulting radiative properties are calculated based on the four-hourly varying meteorological fields. For this forcing calculation, the aerosol concentrations remain the same before, during, and after rain events, although they vary in the IMPACT aerosol calculation that produces the monthly average values that we use in the radiative transfer model. This method provides a reasonable approximation of the radiative forcing calculated using hourly varying aerosol fields (with the difference within 12%) and thus approximates an online calculation [*Penner et al.*, 2011b].

We use two spectrally varying sets of the imaginary part of refractive index (k) for BrC produced from biomass burning/biofuel (Table 2). One is that measured by *Kirchstetter et al.* [2004] and the other is that derived from the averaged absorption per mass (α/ρ) of OC samples in methanol extracts after a semivolatile organic carbon correction [*Chen and Bond*, 2010]. These samples were generated at 210°C from different wood types and different sizes. While other measurements using different methods performed on different fuel types and in different conditions show different refractive indices [e.g., *Chakrabarty et al.*, 2010; *Lack et al.*, 2012; *Saleh et al.*, 2013], their values fall in between those of *Kirchstetter et al.* [2004] and *Chen and Bond* [2010] (Table 3). These two sets of refractive indices therefore provide potential limits to the light-absorbing properties of BrC, although the actual refractive indices of BrC in the atmosphere may be more variable. The refractive indices of residential coal-burning BrC are assumed to be the same as those for biomass-burning BrC, because similar combustion processes occur in these two types of burning [*Andreae and Gelencsér*, 2006]. The choice of refractive index of BrC formed in SOA however is not straightforward since the light-absorbing properties of SOA depend on its precursor type and formation mechanism (e.g., oxidation level and NO_x level) and thus show a wide variance [*Andreae and Gelencsér*, 2006; *Zhang et al.*, 2011; *Nakayama et al.*, 2013;

Table 2. The Imaginary Part of Refractive Index (k) of BrC at Different Wavelengths Used in the Model

Wavelength (nm)	350	400	450	500	550	600	650	700
H-ABS[a]	0.168	0.112	0.063	0.045	0.030	0.017	0.005	0.001
L-ABS[b]	0.0738	0.025	0.0066	0.0024	0.0010	0.0004	0.0002	0.0001

[a]High-absorbing case with k adopted from *Kirchstetter et al.* [2004].
[b]Low-absorbing case with k derived from *Chen and Bond* [2010].

Lambe et al., 2013]. In addition, while laboratory studies by *Sareen et al.* [2013] and *Woo et al.* [2013] have shown that the brown SOA from the aqueous-phase reaction of methylglyoxal becomes white when it is photolyzed, other laboratory measurements [e.g., *Updyke et al.*, 2012] have shown that the reaction with ammonia caused the fresh SOA from biogenic and anthropogenic precursors to become browner. Future work should focus on understanding the different light-absorbing properties for SOA generated from different precursors and its aging. Given this large uncertainty, we therefore use the two sets of refractive indices inferred from *Kirchstetter et al.* [2004] and *Chen and Bond* [2010] to bracket the light absorption of the BrC contained in SOA. The existing measurements of SOA BrC refractive indices reported in the literature [e.g., *Lambe et al.*, 2013; *Nakayama et al.*, 2013; *Saleh et al.*, 2013; *Updyke et al.*, 2012] are within the range of the refractive indices that we use (Table 3). For example, the refractive index of biomass-burning SOA estimated by *Saleh et al.* [2013] and of "humic-like substances" (HULIS) extracted from smoke and air pollution aerosols examined by *Dinar et al.* [2007] are consistent with the refractive index adopted from *Kirchstetter et al.* [2004], the refractive index of HULIS extracted from rural aerosols reported by *Dinar et al.* [2007] lies close to the refractive index inferred from *Chen and Bond* [2010].

The fraction of OA that is light absorbing has varied somewhat in different reports. *Chen and Bond* [2010] reported that methanol-soluble-absorbing OA accounted for more than 92% of the total wood combustion OA. *Kirchstetter et al.* [2004] found that the absorbing OA extracted by acetone accounted for most of the biomass-burning OA. They stated that the remaining unextracted OA could still absorb some small amount of light, although *Chen and Bond* [2010] found that acetone extraction accounted for all of the light absorption. We note however that the organic aerosols produced in the experiments by *Chen and Bond* [2010] were produced by suppressing flames. Nevertheless, we assumed that all of the biomass burning and the biofuel POA is light-absorbing OA. This assumption may need revision however based on further experiments. For fossil-fuel emissions, we assume that only residential coal burning can generate BrC [*Bond et al.*, 1999; *Yang et al.*, 2009], whereas other fossil fuel-produced POA is assumed to be purely scattering. In the IMPACT model, biofuel POA and fossil fuel POA are lumped together and transported as a single tracer (fossil fuel/biofuel POA). To estimate the BrC fraction in fossil fuel/biofuel POA, we use the ratio of their corresponding local emission rates (i.e., divide the emission rate of fossil fuel/biofuel POA by the emission rates of residential coal-burning-generated POA and biofuel POA).

Table 3. The Imaginary Part of Refractive Index of BrC Reported in the Literature

Sample	Wavelength (nm)	Imaginary Part of Refractive Index	Reference
SOA generated from photooxidation of toluene	405	0.0~0.082	*Nakayama et al.* [2013]
SOA generated from photooxidation of toluene	532	0.0~0.017	*Nakayama et al.* [2013]
Biomass-burning particles from the Fourmile Canyon fire near Boulder, Colorado	404	0.07 ± 0.05	*Lack et al.* [2012]
SOA generated in a flow reactor in the absence of NO_x by OH oxidation of gas-phase precursors used as surrogates for anthropogenic, biomass burning, and biogenic emissions	405	1.9×10^{-4}~3.6×10^{-3}	*Lambe et al.* [2013]
Biomass-burning POA	550	0.0055~0.06	*Saleh et al.* [2013]
Biomass-burning SOA	550	0.01~0.05	*Saleh et al.* [2013]
Day and night humic-like substances (HULIS) isolated from the fine fraction of biomass-burning aerosol collected in the Amazon Basin	532	0.0016~0.0019	*Hoffer et al.* [2006]
SOA from glyoxal reactions in aqueous phase	350	0.01 ± 0.02	*Trainic et al.* [2011]
SOA produced through photooxidation of different precursor hydrocarbons such as toluene, d-limonene, and α-pinene in the presence of NO_x and inorganic seed aerosol	350	1×10^{-4}~1×10^{-2}	*Zhong and Jang* [2011]
SOA generated during the photooxidation of toluene and the ozonolysis of α-pinene	350	0~0.088	*Nakayama et al.* [2010]
SOA generated during the photooxidation of toluene and the ozonolysis of α-pinene	532	0~0.037	*Nakayama et al.* [2010]
Tar balls from smoldering combustion of wood	532	0.002~0.008	*Chakrabarty et al.* [2010]
HULIS extracted from filter samples from smoke, air pollution, and rural aerosols	532	0.003~0.05	*Dinar et al.* [2007]

Table 4. Case Description

Case name		H-ABS (High-Absorbing Case)	L-ABS (Low-Absorbing Case)
Biomass-burning POA	BrC fraction	100%	100%
	Refractive index of BrC	Adopted from *Kirchstetter et al.* [2004]	Derived from *Chen and Bond* [2010]
	Size distribution	Majority of the particles have a median radius, $r_g = 0.08\ \mu m$ and a geometric standard deviation, $s_g = 1.4$.	Majority of particles have a median radius, $r_g = 0.08\ \mu m$, and a geometric standard deviation, $s_g = 1.4$.
Fossil fuel/biofuel POA	BrC fraction	The ratio of biofuel and residential coal-burning POA emission rates to the total fossil fuel and biofuel POA emission rates	The ratio of biofuel and residential coal burning POA emission rates to the total fossil fuel and biofuel POA emission rates
	Refractive index of BrC	Adopted from *Kirchstetter et al.* [2004]	Derived from *Chen and Bond* [2010]
	Size distribution	Forty-three percent has $r_g = 0.005\ \mu m$, $s_g = 1.5$ and 50% has $r_g = 0.08\ \mu m$, $s_g = 1.7$.	Forty-three percent has $r_g = 0.005\ \mu m$, $s_g = 1.5$ and 50% has $r_g = 0.08\ \mu m$, $s_g = 1.7$.
SOA	BrC fraction	The same as biomass-burning POA	The same as fossil fuel/biofuel POA
	Refractive index of BrC	Adopted from *Kirchstetter et al.* [2004]	Derived from *Chen and Bond* [2010]
	Size distribution	The same as biomass-burning POA	The same as fossil fuel/biofuel POA

Light-absorbing SOA appears to be ubiquitous in the atmosphere. Light-absorbing SOA is found in aerosols containing nitrated or aromatic aerosols [*Jacobson*, 1999], in humic-like substances (HULIS) formed in heterogeneous reactions [*Limbeck et al.*, 2003; *Gelencsér et al.*, 2003], in "aged" SOA with ammonia [*Updyke et al.*, 2012], in biomass-burning SOA [*Saleh et al.*, 2013], in SOA generated from photooxidation of α-pinene and toluene in the presence of NO_x [*Jaoui et al.*, 2008; *Nakayama et al.*, 2010; *Zhong and Jang*, 2011; *Nakayama et al.*, 2012; *Kim et al.*, 2012], from the reaction of d-limonene with O_3 [*Bones et al.*, 2010], from the photooxidation of phenolic precursors [*Chang and Thompson*, 2010], and from aqueous-phase reactions involving glyoxal and methyglyoxal [*Shapiro et al.*, 2009; *Galloway et al.*, 2009; *Trainic et al.*, 2011]. Since the fraction of SOA that is absorbing is not known with any precision, we made an assumption that 100% of SOA is BrC. We also conducted a sensitivity test assuming the local fraction of BrC in SOA to be the same as that in the fossil fuel/biofuel POA.

The density of both POA and SOA is set to be 1.2 g/cm^3 [*Turpin and Lim*, 2001]. The real part of the refractive index is set to be 1.53. Organic aerosols were treated with a "kappa" factor (a hygroscopicity parameter) of 0.14 for all the source categories for both water uptake as well as droplet formation. The size distribution of OA is prescribed with a superposition of three fixed lognormal distributions [*Wang et al.*, 2009, Table 1]. Specifically, biomass-burning POA is represented by a number distribution with the majority having a median radius, r_g, near 0.08 μm and a geometric standard deviation, s_g, of 1.4; 43% of the fossil fuel/biofuel POA number concentration is represented by a lognormal distribution with $r_g = 0.005\ \mu m$ and $s_g = 1.5$, while 57% is represented by a lognormal distribution with $r_g = 0.08\ \mu m$ and $s_g = 1.7$. For SOA, we assume a lognormal size distribution that is similar to that of the biomass-burning POA. However, if organics mainly condense on smaller aerosols, i.e., on freshly nucleated sulfate aerosols [*Metzger et al.*, 2010], their size might be considerably smaller. Thus, we also examine a second case, where SOA has the same size distribution as that of the fossil fuel/bio fuel POA.

Based on the above discussion, we set up two cases to calculate the direct forcing of POA, SOA, and total OA. A brief description of these two case setups is given in Table 4. For the high-absorbing case (H-ABS), the imaginary part of the refractive index of BrC is adopted from *Kirchstetter et al.* [2004]. All SOA is assumed to be BrC (i.e., light absorbing) and to have the same size distribution as that of the biomass-burning POA. For the low-absorbing case (L-ABS), the imaginary part of the refractive index of BrC is derived from *Chen and Bond* [2010]. The size distribution and the BrC fraction of SOA are assumed to follow those used for fossil fuel/biofuel POA.

Cloud droplet number concentrations were calculated using the cloud droplet activation parameterization of *Abdul-Razzak and Ghan* [2000, 2002]. The size distribution of the nucleated droplet population accounts for the effects of droplet dispersion [*Rotstayn and Liu*, 2003]. The cloud droplet effective radius was used to calculate the cloud optical depth and the first aerosol indirect forcing using an off-line radiative transfer model taken from the National Center for Atmospheric Research (NCAR) Community Atmosphere Model 3 [*Collins et al.*, 2006].

To compute the radiative forcing from organic aerosol deposited in land snow and sea ice, we imported the organic aerosol dry and wet deposition fields calculated in the IMPACT PD and PI runs into two off-line models: the NCAR Community Land Model 4 (CLM4) [*Oleson et al.*, 2010; *Lawrence et al.*, 2011] for the land snow simulation and the Community Ice Code 4 (CICE) [*Hunke and Lipscomb*, 2008; *Holland et al.*, 2012] for the sea ice simulation. Both simulations were run with monthly resolved OA deposition fields and prescribed meteorology data for 1997, consistent with the atmospheric simulations. We generated OA optical properties on the CLM and CICE spectral grids using Mie calculations with identical refractive indices and size distributions as those assumed for the H-ABS and L-ABS atmospheric OA scenarios. Ten different OA species were tracked in these simulations: hydrophilic and hydrophobic brown fossil fuel/biofuel POAs, nonbrown fossil fuel/biofuel POA, brown biomass-burning POA, brown SOA, and nonbrown SOA. Hydrophilic and hydrophobic OAs are differentiated by the number of monolayers of sulfate coating on OA, following *Yun et al.* [2013]. If the number exceeds three, OA is classified as hydrophilic OA. Otherwise, it is classified as hydrophobic OA. Meltwater scavenging ratios for hydrophilic and hydrophobic OA constituents are set to 0.2 and 0.03, respectively, identical to those applied to BC in previous studies [*Flanner et al.*, 2007, 2009; *Holland et al.*, 2012]. For more detailed descriptions of the snow and sea ice treatments of aerosol processes and radiative transfer, readers are referred to *Flanner et al.* [2007], *Oleson et al.* [2010], *Lawrence et al.* [2011], *Holland et al.* [2012], and *Jiao et al.* [2014].

3. Results

3.1. Comparison of Present-Day Simulations With Observations

Previous IMPACT model/measurement comparisons have shown reasonable agreements for O_3, NO_x, and peroxyacetyl nitrate [*Ito et al.*, 2007] as well as POA and SOA [*Lin et al.*, 2012, 2014]. The model mean methane lifetime against OH loss of 7.5 years is at the low end of the range of values (7.1–14 years) reported by Atmospheric Chemistry and Climate Model Intercomparison Project (ACCMIP) models [*Naik et al.*, 2013] and is about 33% lower than the recent observationally derived estimate of 11.2 ± 1.3 years for 2010 [*Prather et al.*, 2012]. The lower estimate in the model suggests that the annual mean model present-day OH abundance is overestimated compared to observations, which may be due to higher-OH sources (e.g., more abundant water vapor) and/or lower-OH sinks in the model. For example, the IMPACT model showed a negative bias of CO in the northern hemisphere compared to the Measurements of Pollution in the Troposphere CO data [*Ito*, 2011]. Thus, an increase of CO sources in the model would improve both OH and CO. Nevertheless, future work is needed to examine the OH budget in the model.

We also compare our modeled single scattering albedo (SSA) and aerosol absorption optical depth (AAOD) at 550 nm with those retrieved from the AERONET data provided by S. Kinne (Max Planck Institute for Meteorology). The AERONET retrieved SSA data are from the official version 2.0 product with an adjustment to reduce a positive bias resulting from the removal of SSA data for low-AOD cases (i.e., cases with AOD less than 0.33). This adjustment replaced the missing refractive index data in the version 2.0 product with the data from the version 1.5 data product, which is expected to reduce the positive bias to some extent but to introduce a larger uncertainty (S. Kinne, personal communication, 2012). The monthly mean for the AERONET retrieved data is calculated for 1996–2011. Globally, the normalized mean bias between the monthly mean modeled and the observed SSA is 1.91% for H-ABS case and 3.96% for L-ABS case. The predicted SSA for the H-ABS case is in good agreement with the observed SSA over all regions except for Europe, while the model for the L-ABS case tends to overpredict SSA (Figure 1 and Table 5). However, both the H-ABS case and the L-ABS case underestimate the observed AAOD, especially over biomass-burning regions (e.g., South Asia, south Africa, and South America) (Figure 2 and Table 5). The high-absorbing BrC assumption helps to enhance the predicted AAOD but not enough to fill the large gap between the simulation and the observations. The negative bias of AAOD shown in the model suggests that the model probably still underpredicts the source or/and overpredicts the sink of absorbing aerosols. In addition, more scattering aerosols (e.g., pure scattering OA) would be needed in order to maintain the present agreement with the observed SSA.

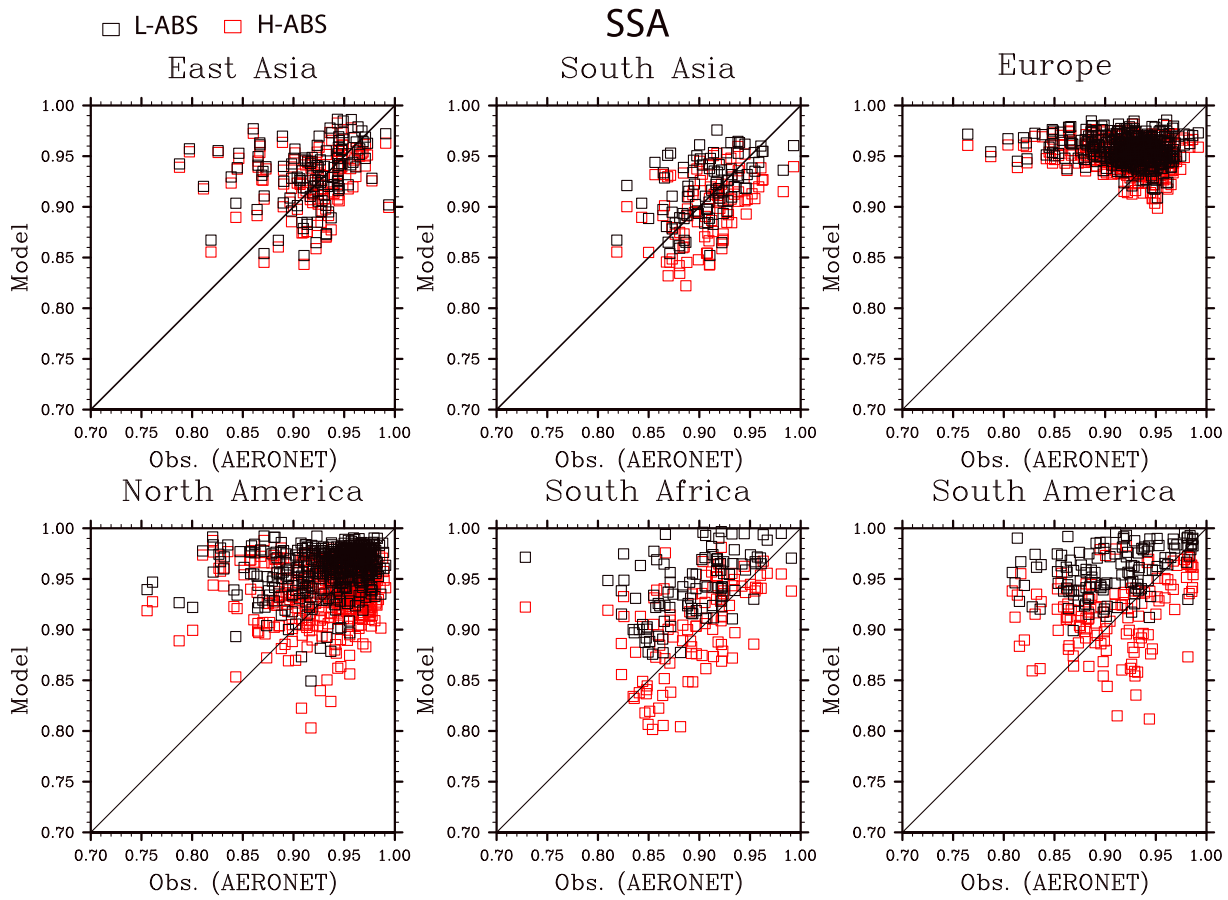

Figure 1. Monthly averaged single scattering albedo (SSA) comparison between the model simulations and the AERONET retrieved data. The black squares are for the L-ABS case, and the red squares are for the H-ABS case. The solid line represents a perfect match between the simulation and observations.

Figure 3 shows the comparison of predicted aerosol absorption Ångström exponent (AAE) at 440–675 nm with AAE derived from AERONET data. The AAE indicates how the aerosol absorption varies with wavelength and is calculated from the equation given below.

$$\mathrm{AAE} = -\log\left(\frac{\mathrm{AAOD}_{675\mathrm{nm}}}{\mathrm{AAOD}_{440\mathrm{nm}}}\right) \Big/ \log\left(\frac{675}{440}\right)$$

As shown in Figure 3, the model slightly underestimates the observed AAE in the L-ABS case, while it predicts a stronger AAE in the H-ABS case over all the regions. This overprediction implies that the wavelength dependence of BrC absorption adopted from *Kirchstetter et al.* [2004] may be stronger than that in the real atmosphere or that the model overestimates the contribution of BrC to the total aerosol absorption.

3.2. Changes in POA and SOA Between PD and PI Simulations

Figure 4 shows the change in the column burden of biomass-burning POA and fossil fuel/biofuel POA between the PD and PI simulations for the simulation using the *Lin et al.*'s [2014] case 5 model. The largest

Table 5. The Geometric Mean Ratio Between the Modeled SSA and AAOD and the Observed SSA and AAOD From AERONET Data for Both the H-ABS Case and the L-ABS Case[a]

		East Asia	South Asia	Europe	North America	South Africa	South America
SSA	H-ABS	1.01	0.99	1.04	1.00	1.01	1.01
	L-ABS	1.02	1.01	1.04	1.03	1.05	1.06
AAOD	H-ABS	0.81	0.48	0.67	0.83	0.34	0.32
	L-ABS	0.79	0.45	0.65	0.60	0.22	0.19

[a]A value larger than 1 indicates that the model tends to overestimate the observations, while a value smaller than 1 indicates the opposite tendency.

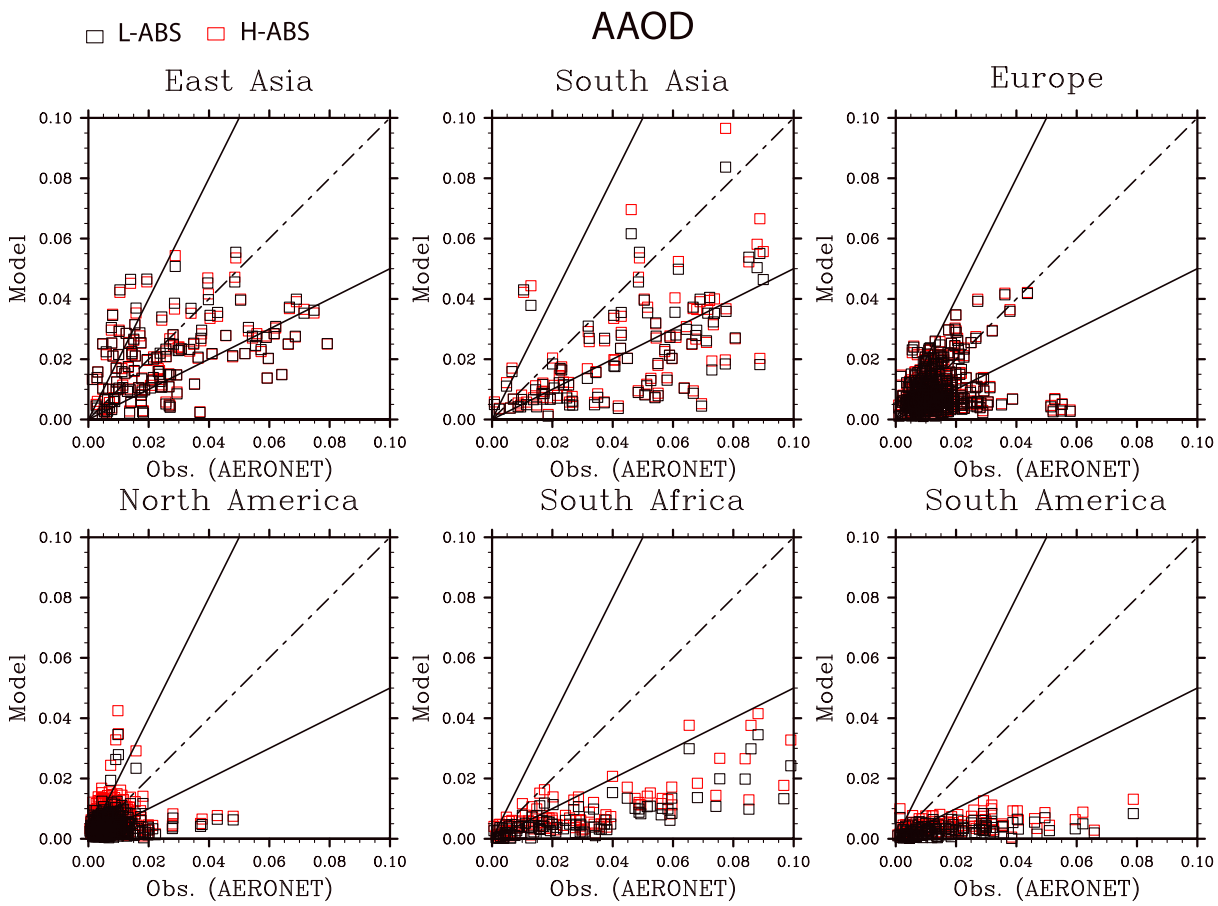

Figure 2. Monthly averaged aerosol absorption optical depth (AAOD) comparison between the model simulations and the AERONET retrieved data. The black squares are for the L-ABS case, and the red squares are for the H-ABS case. The dashed line represents a perfect match between the simulation and the observation (1:1 ratio), and the solid lines are the 2:1 and 1:2 ratios, i.e., indicating agreement within a factor of 2.

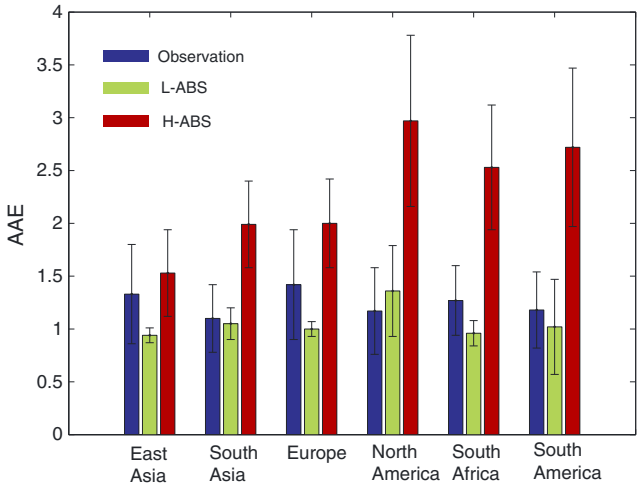

Figure 3. Comparison of regional monthly averaged aerosol absorption Ångström exponent (AAE) between the model simulations and the AERONET retrieved data. The error bars stand for the standard deviation of AAE over each region.

change in biomass-burning POA occurs in central Africa, South Asia, and north Australia, while a significant increase of fossil fuel/biofuel POA occurs in eastern and southern Asia. There is a weak decrease of fossil fuel/biofuel POA in central and eastern Europe as well as in eastern North America. This is due to the decreased biofuel usage in those regions since PI times. The global mean POA burden increases from 0.26 Tg in PI to 0.77 Tg in PD (Tables 6 and 7).

The change in emissions from PI to PD leads to changes in the levels of oxidants (e.g., OH and O_3), which are important for the oxidation of VOC and therefore for the formation of SOA. As a result of the increase in emissions, there is an increase of a factor of 2.5 in the level of boundary layer NO_x, while the isoprene

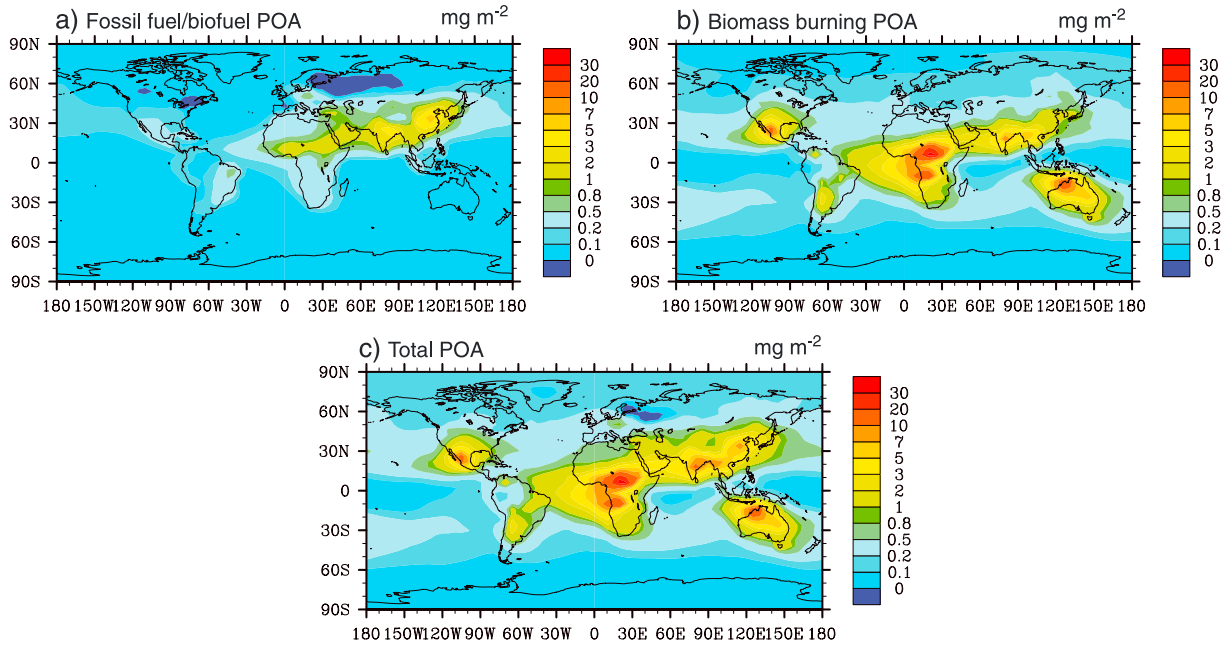

Figure 4. (a–c) The change in the annual mean column burden of POA between the PD and PI conditions.

concentration decreases by 14% (Table 6). These changes result in an increase of boundary layer ozone of 52%, while there is a decrease in the global average boundary layer OH of 10%, driven mainly by the changes in CO (increase of a factor of 2.2) and CH_4 (increase of a factor of 2.1). Over source regions, however, there is an increase in OH that is associated with the increase in NO_x, which is largest in the midlatitude northern hemisphere (Figure 5). There is also a decrease in the global average boundary layer isoprene between PD and PI of 14% caused by the increases in OH over the continents, the increase in O_3 [see also *Tsigaridis et al.*, 2006], and an increase in NO_3 between the PD and PI simulations of 262%. There is still substantial uncertainty on how the OH level has changed since PI times. Previous models have shown that the change in the tropical mean OH level since PI times could range from an increase of 15% to a decrease of 33% [*Naik et al.* [2013], and references therein]. The tropical mean OH concentration is decreased by 17% since PI times in the model, the magnitude of which is larger than the mean value of ACCMIP models (−0.6%) [*Naik et al.*, 2013]. The larger decrease than that reported by ACCMIP models can be mainly attributed to the stronger CO increase and smaller NO_x increase in the model compared to those predicted by ACCMIP models (Table 6).

The change in isoprene and oxidants alone however cannot fully explain the change in SOA. The boundary layer concentrations of SOA formed from glyoxal and methylglyoxal increase by 82%, since preindustrial times, primarily as a result of the increased sulfate aerosol surface area, while the concentrations of gas-phase glyoxal and methylglyoxal, most of which are formed from the OH-initiated oxidation of isoprene [*Fu et al.*, 2008], change very little in the boundary layer. The SOA formed from epoxide also increases as a result of the increased surface area of sulfate, by a factor of 1.2 in the boundary layer, even though the gas-phase epoxide concentration decreases by 22.6% as a result of the significant increase of NO. The increase of NO causes RIO2 (organic peroxy radicals from isoprene) to react more with NO and therefore less with HO_2 to form the epoxide [*Lin et al.*, 2012]. On the other hand, the concentration of PRN2 (isoprene-hydroxy-nitrate, the greatest contributor to the SOA formed from organic nitrates and peroxides), which mainly comes from the reaction of RIO2 with NO [*Lin et al.*, 2012], is enhanced by 46.3% in the boundary layer. This increase, together with the increase in the abundance of POA, upon which the SOA can partition, causes the concentration of SOA from organic nitrates and peroxides to double in the boundary layer.

Table 7 shows the global production rate and burden of SOA for PD and PI conditions. The global average formation of SOA is dominated by biogenic VOCs even for PD conditions. The SOA formed from anthropogenic VOCs (mainly aromatics) only accounts for 7.6% of the total SOA production. Although the biogenic VOC emissions do not change, the biogenic SOA production rate increases by 24.9 Tg/yr (80.0%) as a result of the anthropogenic emissions and reactions discussed here. The distribution of the changes in the total SOA at the

Table 6. Burden in the Boundary Layer (Below Approximately 900 hPa in the Model), in the Troposphere (Below Approximately 200 hPa in the Model), or in the Whole Atmosphere for the PD and PI Conditions and Their Relative Difference

				Other Work	
Species	PD	PI	(PD-PI)/PI	PD (Tg)	(PD-PI)/PI
OH in the boundary layer	1.78×10^{-5} Tg	1.98×10^{-5} Tg	−10.1%		
	1.45×10^{6} (mol cm^{-3})	1.61×10^{6} (mol cm^{-3})	−9.9%		
OH in the troposphere	2.33×10^{-4} Tg	2.82×10^{-04} Tg	−17.4%		-0.6 ± 8.8%[a]
	14.3×10^{5} (mol cm^{-3})	17.3×10^{5} (mol cm^{-3})	−17.3%	$11.1\pm1.6\times10^{5}$ (mol cm^{-3})[a]	
NO_x in the boundary layer	1.06×10^{-1} Tg	4.30×10^{-2} Tg	146.5%		over 300%[b]
	142.0 parts per trillion (ppt)	57.8 ppt	145.7%		
NO_x in the troposphere	3.15×10^{-1} Tg	1.96×10^{-1} Tg	60.7%		108.0 ± 75.4%[a]
	52.2 ppt	33.2 ppt	57.2%		
CO in the boundary layer	85.6 ppb	38.8 ppb	120.6%		
	40.2 Tg	18.2 Tg	120.9%		
CO in the troposphere	287.2 Tg	136.2 Tg	110.9%		89.1 ± 18.6%[a]
	72.9 ppb	34.5 ppb	111.3%		
CH_4 (global)	4806 Tg	2262 Tg	112.4%	4813 ± 81 Tg[a]	120.9%[a]
	1.7 ppm	0.8 ppm	112.5%		
O_3 in the boundary layer	25.5 Tg	16.8 Tg	51.8%		74%[b]
	31.6 ppb	20.8 ppb	51.9%		
O_3 in the troposphere	339 Tg	243 Tg	39.5%	337 ± 23 Tg[c]	29% ± 17%[c]
	50.4 ppb	36.5 ppb	38.1%		
Isoprene in the boundary layer	1.13×10^{-1} Tg	1.31×10^{-1} Tg	−13.7%		−42%[b]
	98.8 ppt	114.9 ppt	−14.0%		
NO_3 in the boundary layer	8.36×10^{-4} Tg	2.31×10^{-4} Tg	262%		
	0.8 ppt	0.2 ppt	300%		
HO_2 in the boundary layer	3.53×10^{-3} Tg	3.12×10^{-3} Tg	13.1%		
	6.4 ppt	5.6 ppt	14.3%		
Sulfate in the boundary layer	2.76×10^{-1} Tg	8.70×10^{-2} Tg	217%		
Sulfate (global)	2.72 Tg	1.12 Tg	143%	1.4 Tg[d]	338%[d]
				1.05 Tg[b]	160%[b]
				1.8 Tg[e]	114%[e]
POA in the boundary layer	2.13×10^{-1} Tg	7.52×10^{-2} Tg	183%		
POA (global)	0.77 Tg	0.26 Tg	196%	1.27 Tg[d]	1220%[d]
				0.6 Tg[b]	120%[b]
				1.41 Tg[e]	178%[e]
				1.2 Tg[f]	991%[f]
PRN2 in the boundary layer	5.52×10^{-2} Tg	4.05×10^{-2} Tg	46.3%		
	14.4 ppt	10.5 ppt	37.1%		
Glyoxal in the boundary layer	1.39×10^{-2} Tg	1.58×10^{-2} Tg	−12.0%		
	14.3 ppt	16.2 ppt	−11.7%		
Methylglyoxal in the boundary layer	2.79×10^{-2} Tg	2.57×10^{-2} Tg	8.6%		
	23.7 ppt	21.2 ppt	11.8%		
Epoxide in the boundary layer	5.24×10^{-2} Tg	6.77×10^{-2} Tg	−22.6%		
	26.9 ppt	34.8 ppt	−22.7%		
SOA (global)	0.99 Tg	0.59 Tg	68%	0.33 Tg[d]	43%[d]
				0.8 Tg[b]	25%[b]
				0.5–0.7 Tg[e]	56–59%[e]
				0.19 Tg[f]	217%[f]

[a] ACCMIP models [*Naik et al.*, 2013].
[b] *Tsigaridis et al.* [2006].
[c] ACCMIP models [*Young et al.*, 2013].
[d] *Liao and Seinfeld* [2005].
[e] *Hoyle et al.* [2009].
[f] *Chung and Seinfeld* [2002].

surface and for the total column are shown in Figure 6. The largest increase in SOA occurs over industrialized areas, such as Southeast Asia, Europe, and the eastern U.S., where the increases of NO_x, sulfate, and OH account for most of the increase in SOA. Large increases in SOA are also evident in South America and West Africa, where the increase in biomass-burning POA and sulfate are the major source of the SOA increase. Increases in

Table 7. Summary of the Total Burden and Source of POA and SOA for Present-Day and Preindustrial Conditions

	SOA		POA	
	PD	PI	PD	PI
Burden (Tg)	0.99	0.59	0.77	0.26
Total source (Tg/yr)	60.4	31.2	63.1	23.0
Total biogenic source (Tg/yr)	56.1	31.2	-	-
Total anthropogenic source (Tg/yr)	4.3	0.0	-	-

SOA over the ocean, in the outflow of East Asia, Africa, and South America, can also be seen in the column burden (Figure 6b).

3.3. Direct Forcing Due to the Change in POA and SOA

As shown in Figure 7, the clear-sky POA direct radiative forcing at the top of atmosphere (TOA) is predominately negative over the globe, exerting a cooling effect on the climate. Although POA would normally be internally mixed with BC in the atmosphere, here we examine the forcing of POA alone to give us a first-order estimate of its independent contribution to forcing. The geographical distribution of direct forcing basically follows the pattern of burden increase of POA (Figure 4), having large values in central Africa, South and East Asia, and southwestern U.S. It is notable that in the high-absorbing case, there is weak warming over the Himalayan mountains, which are covered by snow/ice and thus have a high-albedo surface, allowing the upward radiation reflected by the high-albedo surface to be further absorbed by POA. In the high-absorbing case (H-ABS), the global averaged clear-sky forcing at the TOA is $-0.20\,W/m^2$ (Table 9), while the all-sky forcing at the TOA is $-0.06\,W/m^2$. The weaker cooling under all-sky conditions is due to enhanced absorption by the POA at elevated levels above reflective clouds. The forcing at the surface is much stronger than that at the TOA (Figure 7 and Table 9), which is due to the absorption by BrC in the atmosphere. The global mean all-sky absorption in the atmosphere amounts to $0.25\,W/m^2$ (Table 9). Not surprisingly, this absorption decreases to $0.14\,W/m^2$ in the low-absorbing case (L-ABS). The global mean forcing at the TOA becomes $-0.11\,W/m^2$ for all-sky conditions and $-0.23\,W/m^2$ for clear-sky conditions.

The difference in SOA between the PD and PI conditions causes a global annual average direct radiative forcing of $-0.37\,W\,m^{-2}$ for clear-sky and $-0.12\,W\,m^{-2}$ for all-sky conditions for the high-absorbing case (Table 8). For the low-absorbing case, the direct forcing is $-0.59\,W\,m^{-2}$ for clear-sky and $-0.31\,W\,m^{-2}$ for all-sky conditions. *Hoyle et al.* [2009] estimated the direct radiative forcing of anthropogenic SOA to be -0.06~$-0.09\,W\,m^{-2}$, which corresponded to an increase in the rate of SOA production of 18–26 Tg/yr. *Spracklen et al.* [2011] reported a direct forcing of $-0.26 \pm 0.15\,W\,m^{-2}$, resulting from a global anthropogenic SOA production rate that ranged from 40 Tg/yr to 160 Tg/yr. SOA was treated as a pure scattering aerosol in these two studies, but here we account for its absorbing properties [*Kirchstetter et al.*, 2004; *Chen and Bond*, 2010], which reduces the amount of negative forcing at the TOA, since some of the radiation that would be reflected is absorbed. This absorption also reduces the short wave radiative flux reaching the surface, leading to a stronger negative surface radiative forcing compared to that at the TOA (shown below) for both clear-sky and all-sky conditions.

The distribution of the direct radiative forcing at the TOA for the all-sky and clear-sky conditions and the all-sky radiative forcing at the surface associated with these changes in SOA is shown in Figure 8. The direct forcing at the TOA is dominated by changes of aerosols in the northern hemisphere with peaks over the source areas: southeastern Asia, central Africa, eastern U.S., and Europe. The absorption by SOA within the atmospheric column is given by the difference between the forcing at the TOA and the surface. Assuming

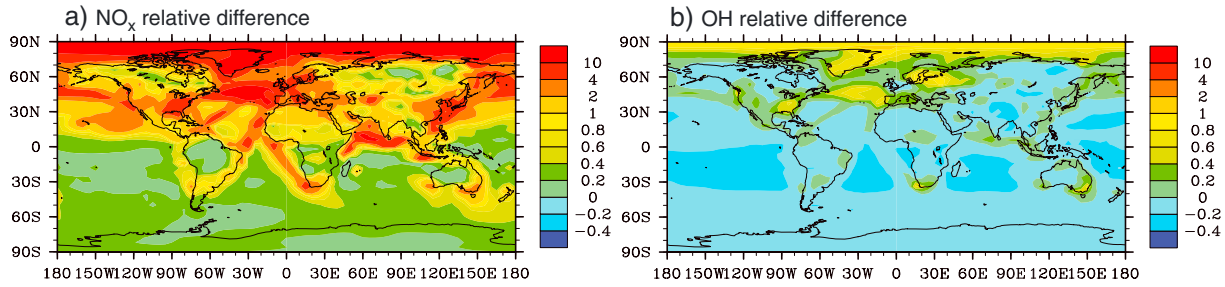

Figure 5. The relative difference (i.e., (PD-PI)/PI) between the PD and PI conditions for (a) NO_x and (b) OH in the boundary layer.

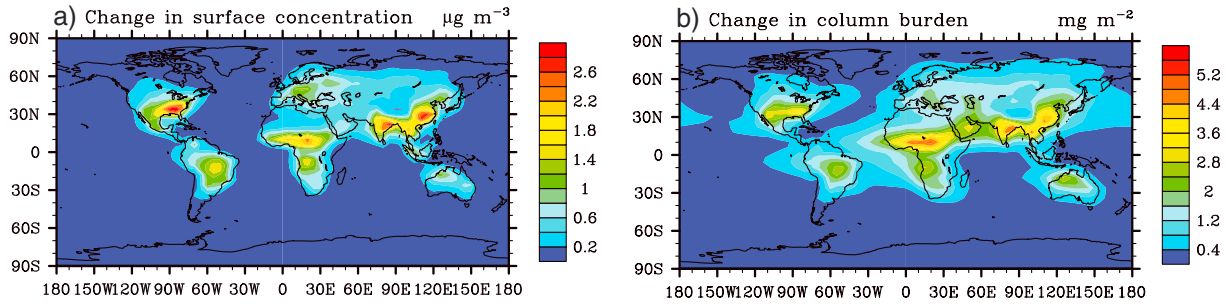

Figure 6. The change in the annual mean SOA concentration between the PD and PI conditions. (a) Changes at the surface and (b) changes for the total column integrated mass per square meter.

that all of the SOA is slightly absorbing and has a larger refractive index, as in the high-absorbing case, leads to a positive direct forcing at the TOA for all-sky conditions over the Himalayan mountains and off the west coast of Africa and South America (Figure 8c), where low clouds increase the amount reflected below the aerosol layer leading to more absorption. Absorption and a positive forcing are also evident over the areas with high albedo from snow and ice surfaces in the polar regions.

The annual global mean all-sky direct forcing of POA at the TOA for both the high-absorbing and low-absorbing cases (Table 9) is weaker than the mean POA direct forcing of $-0.14\ W/m^2$ estimated by Aerosol Comparisons between Observations and Models (AEROCOM) phase I models [*Schulz et al.*, 2006], which assumed POA to be nonabsorbing. As shown in Table 9, it is also less negative than the total OA forcing values reported by *Liao and Seinfeld* [2005], *Ming et al.* [2005], and *Ocko et al.* [2012], which were mainly associated with POA since POA dominated OA. The global mean all-sky direct forcing for changes in both POA and SOA, at the TOA decreases to $-0.14\ W/m^2$ for the high-absorbing case and to $-0.40\ W/m^2$ for the low-absorbing case. The inclusion of SOA therefore increase the negative OA forcing at TOA (cooling the climate) by 133.3% in high-absorbing case and by around a factor of 3 in the low-absorbing case. The cooling effect of total OA (POA + SOA) in both cases is stronger than the mean estimate by AEROCOM phase I models [*Schulz et al.*, 2006], and the forcing in the low-absorbing case is stronger than the forcing reported by non-AEROCOM models [e.g., *Liao and Seinfeld*, 2005; *Ming et al.*, 2005; *Ocko et al.*, 2012]. This is primarily due to the predicted large change in SOA in this model.

Figure 9 summarizes the direct radiative forcing estimates in this paper and compares them to the estimates in other papers. The forcings of POA estimated in this work are weaker (less negative) than those estimated by the AEROCOM phase I models. Our SOA forcing estimates are stronger than those obtained in other models but within the range of estimates based on SOA constrained by aerosol mass spectrometer (AMS) measurements [*Spracklen et al.*, 2011]. Compared to the forcing estimates of the total OA, our H-ABS and L-ABS estimates both show a stronger cooling than the low end and high end of the range estimated by previous models, respectively.

The global mean all-sky direct forcing resulting from the change in BC since PI times is predicted to be $0.34\ W/m^2$ in the model (Table 9). Adding this with the total OA all-sky forcing gives a total carbonaceous aerosol (BC + OA) direct radiative forcing of $0.20\ W/m^2$ for the high-absorbing case and $-0.07\ W/m^2$ for the low-absorbing case. The IPCC Fifth Assessment Report (AR5) report [*IPCC*, 2013] gave a global and annual mean direct radiative forcing due to aerosol-radiation interaction between 1750 and 2011 of four carbonaceous aerosol components: BC from fossil fuel and biofuel, POA from fossil fuel and biofuel, BC and POA from biomass burning, and SOA. The direct radiative forcing for the sum of these four components in AR5 equals $0.28\ W/m^2$. Our result is slightly smaller for the high-absorbing case but of opposite sign for the low-absorbing case.

The global mean all-sky atmospheric absorption due to the change in the total OA is $0.57\ W/m^2$ in the high-absorbing case and $0.22\ W/m^2$ in the low-absorbing case (Table 9 and Figure 10). This is compared to a global mean absorption of $0.1\sim0.25\ W/m^2$ in the atmosphere due to BrC associated with biomass burning and biofuel burning reported by *Feng et al.* [2013]. *Ming et al.* [2005] reported an atmospheric absorption of 0.29 W/m2 caused by the change in the total OA from PI to PD by assuming that the imaginary part of the refractive index of OA is 0.006. The change in BC leads to a global mean all-sky atmospheric absorption of

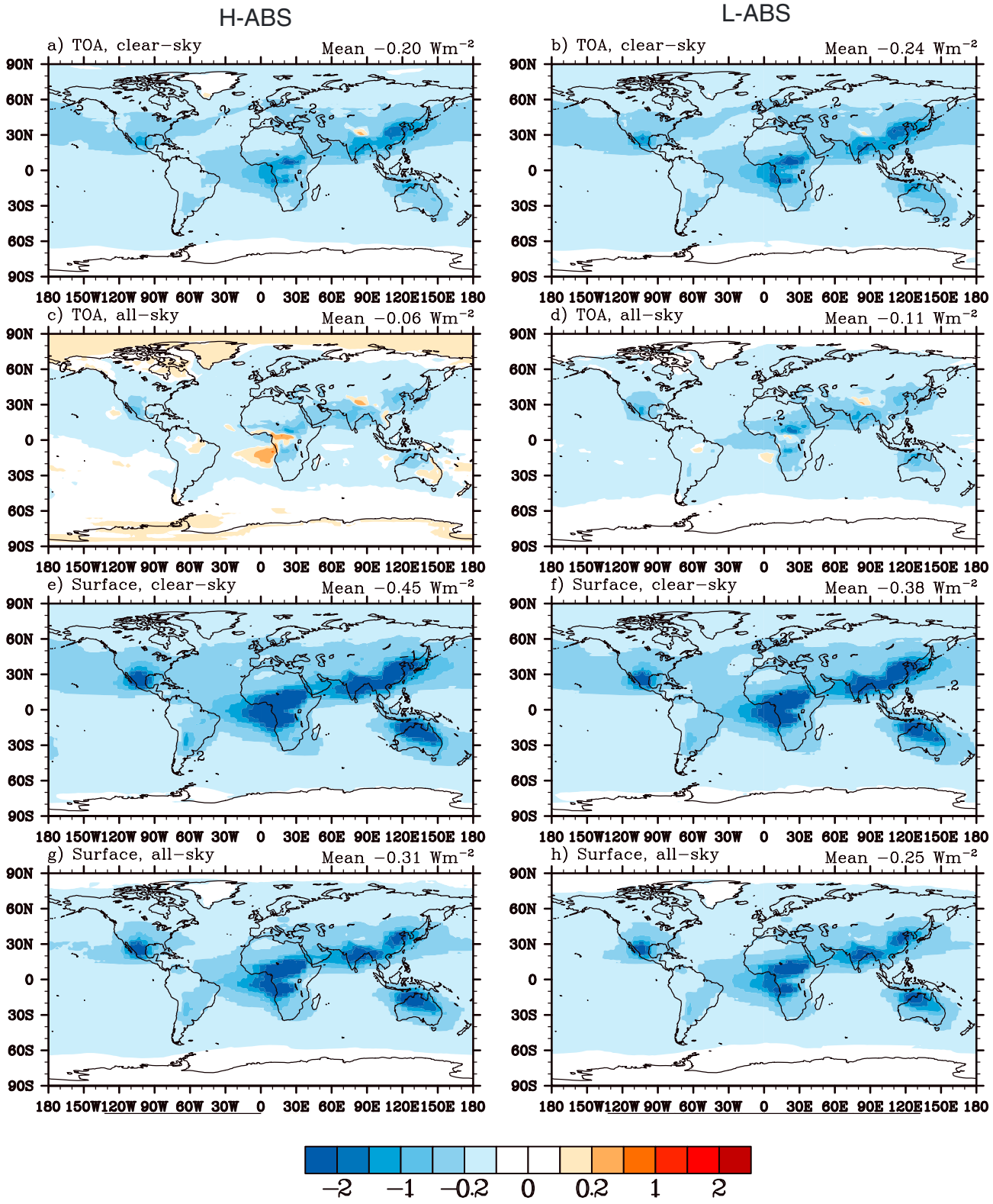

Figure 7. The direct forcing due to the change of POA between the PD and PI conditions at the TOA for (a and b) clear-sky and (c and d) all-sky conditions and at the surface in (e and f) clear-sky and (g and h) all-sky conditions. Figure 7 (left column) shows the high-absorbing case (H-ABS), while Figure 7 (right column) shows the low-absorbing case (L-ABS).

Table 8. Summary of the Estimated TOA and Surface Forcing (W m^{-2}) in Different Simulations Due to the Change of SOA

	Direct Forcing					Other Work	
Case Name	TOA Clear Sky	TOA All Sky	Surface Clear Sky	Surface All Sky	Indirect Forcing	TOA All Sky	Indirect Forcing
H-ABS[a]	−0.37	−0.12	−0.58	−0.35	−0.29	−0.01~−0.04[b]	−0.36~−0.74[d]
L-ABS[a]	−0.59	−0.31	−0.62	−0.35	−0.22	−0.06~−0.09[c] −0.41~−0.11[d]	

[a]H-ABS: high-absorbing case; L-ABS: low-absorbing case.
[b]From other models in AEROCOM phase II [*Myhre et al.*, 2013].
[c]*Hoyle et al.* [2009].
[d]*Spracklen et al.* [2011].

0.82 W/m^2 in the model (Table 9). Thus, the atmospheric absorption caused by the change in BrC in the high-absorbing case accounts for 70% of that caused by the change in BC, and this fraction decreases to 27% in the low-absorbing case. Summing the absorption of BC and BrC, the global mean atmospheric absorption is 1.39 W/m^2 for the high-absorbing case and 1.04 W/m^2 for the low-absorbing case. *Liao and Seinfeld* [2005] estimated an all-sky atmospheric absorption of 1.59 or 2.43 W/m^2 caused by anthropogenic aerosols (including BC), depending on whether the aerosols are internally or externally mixed. *Myhre et al.* [2013] give a mean value of 0.75 W/m^2 for the atmospheric absorption due to all the anthropogenic aerosols based on the AEROCOM phase II models.

3.4. First Indirect Forcing Due to the Change in SOA

Figure 11 shows the first indirect effect at the TOA due to the increased SOA since preindustrial times. The spatial distribution of the forcing is determined by the change in the cloud drop number concentrations, which is primarily due to the change in the total particle number. The case with only an accumulation mode for the size distribution shows a stronger indirect forcing than that for the case that assumes that SOA includes a nucleation mode for 43% of the particles. The global mean indirect forcing is $-0.29\,\mathrm{W\,m^{-2}}$ for the accumulation mode case and $-0.22\,\mathrm{W\,m^{-2}}$ for the nucleation plus accumulation mode case (Table 8). All of our estimates are smaller than the values reported by *Spracklen et al.* [2011] for the indirect forcing by so-called "anthropogenically controlled SOA" that was assumed to be spatially similar to anthropogenic CO emissions (i.e., -0.36 to $-0.74\,\mathrm{W\,m^{-2}}$), based on fitting the results of a global chemical transport model to aerosol mass spectrometer (AMS) observations.

3.5. Radiative Forcing of OA in Land Snow and Sea Ice

Table 10 summarizes the radiative forcing of POA, SOA, total OA, and BC deposited in land snow and sea ice. For the high-absorbing case, the calculated global and annual mean radiative forcing caused by OA in land snow is $2.5\times10^{-3}\,\mathrm{W\,m^{-2}}$, and the forcing of OA in sea ice is $5.5\times10^{-4}\,\mathrm{W\,m^{-2}}$. For the sake of a comparison, we also predict the forcing of BC in land snow and sea ice. BC in land snow and sea ice are shown to cause forcings of $1.2\times10^{-2}\,\mathrm{W\,m^{-2}}$ and $9.9\times10^{-4}\,\mathrm{W\,m^{-2}}$, respectively. *Bond et al.* [2013] gave a best estimate of $3.5\times10^{-2}\,\mathrm{W\,m^{-2}}$ for industrial era adjusted forcing by BC in snow and a best estimate of $1.1\times10^{-2}\,\mathrm{W\,m^{-2}}$ for industrial era forcing by BC in sea ice, based on the analysis of a suite of model studies. Here "adjusted" forcing includes the alteration of radiative forcing because of the "rapid adjustments in snow grain size and surface snow BC concentrations due to the changes in sublimation and melt rates resulting from the initial snow albedo reduction due to BC" [*Bond et al.*, 2013]. These effects are also included in the model framework applied here and affect forcing primarily through melt-induced accumulation of impurities near the snow surface. In the high-absorbing case, OA contributes a forcing on snow and sea ice 7–24% as large as that of BC, based on the range of BC forcings derived here and by *Bond et al.* [2013]. We estimate smaller BC forcing on snow in this study because (1) our model produces less high-latitude BC deposition than previous studies assessed by *Bond et al.* [2013] (e.g., present-day BC deposition north of 50°N is only 32% and 44% as large as that simulated by *Flanner et al.* [2007] and *Flanner et al.* [2009], respectively), (2) the off-line land simulations applied here produce less Asian snow cover than the coupled land-atmosphere simulations used previously [*Flanner et al.*, 2007, 2009], and (3) our simulations produce negative forcing over a substantial portion of eastern Europe and western Asia, associated with decreased BC emissions in this

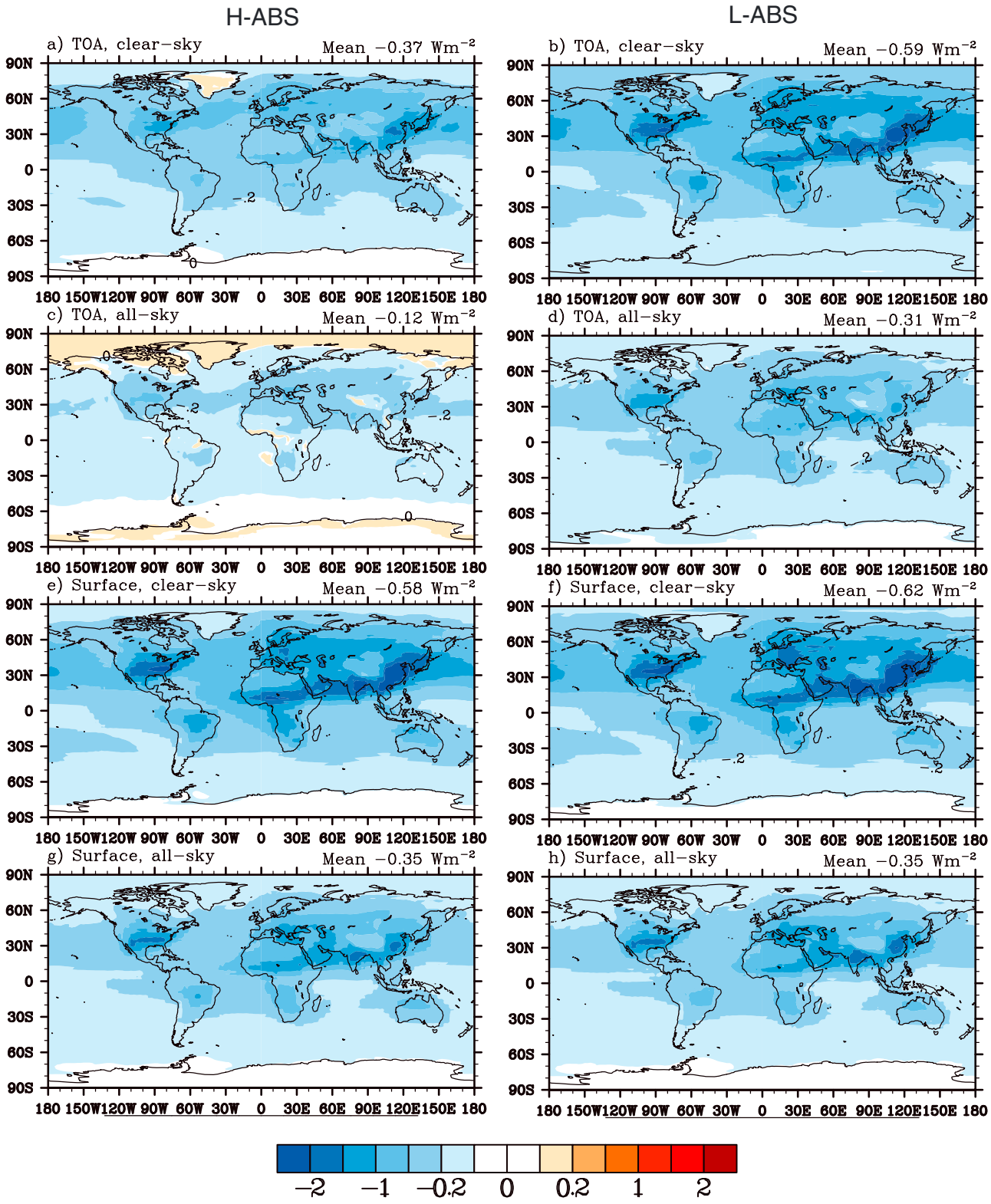

Figure 8. The direct forcing due to the change of SOA between the PD and PI conditions at the TOA for (a and b) clear-sky and (c and d) all-sky conditions and at the surface in (e and f) clear-sky and (g and h) all-sky conditions. Figure 8 (left column) shows the high-absorbing case (H-ABS), while Figure 8 (right column) shows the low-absorbing case (L-ABS).

Table 9. Summary of the Estimated Forcing ($W m^{-2}$) in Different Simulations Due to the Change of POA and Total OA

		Direct Forcing					Other Work	
	Case Name	TOA Clear Sky	TOA All Sky	Surface Clear Sky	Surface All Sky	Atmospheric Absorption All Sky	TOA All Sky	Atmospheric Absorption All Sky
POA	H-ABS	−0.20	−0.06	−0.45	−0.31	0.25	−0.14[a]	0.1~0.25[g]
	L-ABS	−0.23	−0.11	−0.38	−0.25	0.14		
Total OA	H-ABS	−0.54	−0.14	−1.10	−0.71	0.57	−0.23[b]	0.29 [d]
	L-ABS	−0.82	−0.40	−1.03	−0.62	0.22	−0.27[c]	
							−0.34[d]	
							−0.06[e]	
BC		0.23	0.34	−0.61	−0.48	0.82	0.71 (0.08–1.27)[f]	
BC + OA	H-ABS	−0.31	0.20	−1.71	−1.19	1.39		1.59~2.43[bj]
	L-ABS	−0.59	−0.07	−1.64	−1.10	1.04		1.22[hj]
								0.75[ij]

[a]Mean AEROCOM phase I value [*Schulz et al.*, 2006].
[b]*Liao and Seinfeld* [2005].
[c]*Ocko et al.* [2012].
[d]*Ming et al.* [2005].
[e]*Jacobson* [2001].
[f]*Bond et al.* [2013].
[g]*Feng et al.* [2013].
[h]*Takemura et al.* [2005].
[i]Mean of AEROCOM phase II models [*Myhre et al.*, 2013].
[j]These values are reported as atmospheric absorption due to the change in total aerosol since PI times.

region. Among the OA constituents in snow and ice, the contribution to forcing from SOA is larger than that from POA. When we use the smaller imaginary part of the refractive index for OA and assume that less SOA is light absorbing, the albedo effect of OA decreases to 9.0×10^{-4} W m^{-2} in land snow and 1.6×10^{-4} W m^{-2} in sea ice. The radiative forcing of OA in land snow and sea ice declines to 8% of that of BC as calculated in our model and to roughly 2% of the BC forcing estimated by *Bond et al.* [2013]. In contrast to the high-absorbing case, POA plays a more important role in reducing snow and ice albedo in the low-absorbing case than SOA does. We also calculated the all-sky TOA radiative forcing of the total OA in the atmosphere over high-latitude areas (50°N to 90°N and 60°S to 90°S) and over Tibetan Plateau (30°N to 40°N and 70°E to 90°E). The mean forcings in the high-absorbing case are −0.03 W/m^2 and −0.21 W/m^2. The sign of these forcings is opposite to the forcing of the total OA in snow and sea ice, and the magnitude is stronger than that in the snow and sea ice.

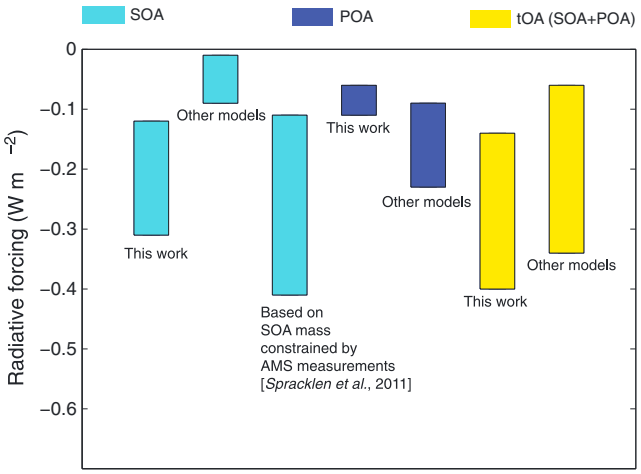

Figure 9. Comparison of the all-sky TOA direct forcing estimates in this work with other models. The specific values for the forcing estimated by other models and their references are given in Table 8 and Table 9.

Figure 12 depicts the global distribution of the annual mean radiative forcing by OA in land snow and sea ice. The distribution reflects the combination of anthropogenic OA concentrations in snow, snow cover, and surface-incident solar flux. The forcing is distributed over high-latitude areas (40°N to 90°N and 60°S to 90°S). While the POA from ocean sources contributes most of the forcing in the southern hemisphere, fossil fuel, biofuel, and biomass-burning POA and SOA play an important role in the northern hemisphere. There is a large forcing over Greenland primarily because of its perennial snow cover. There is a strip of negative OA forcing over central and eastern Europe due to

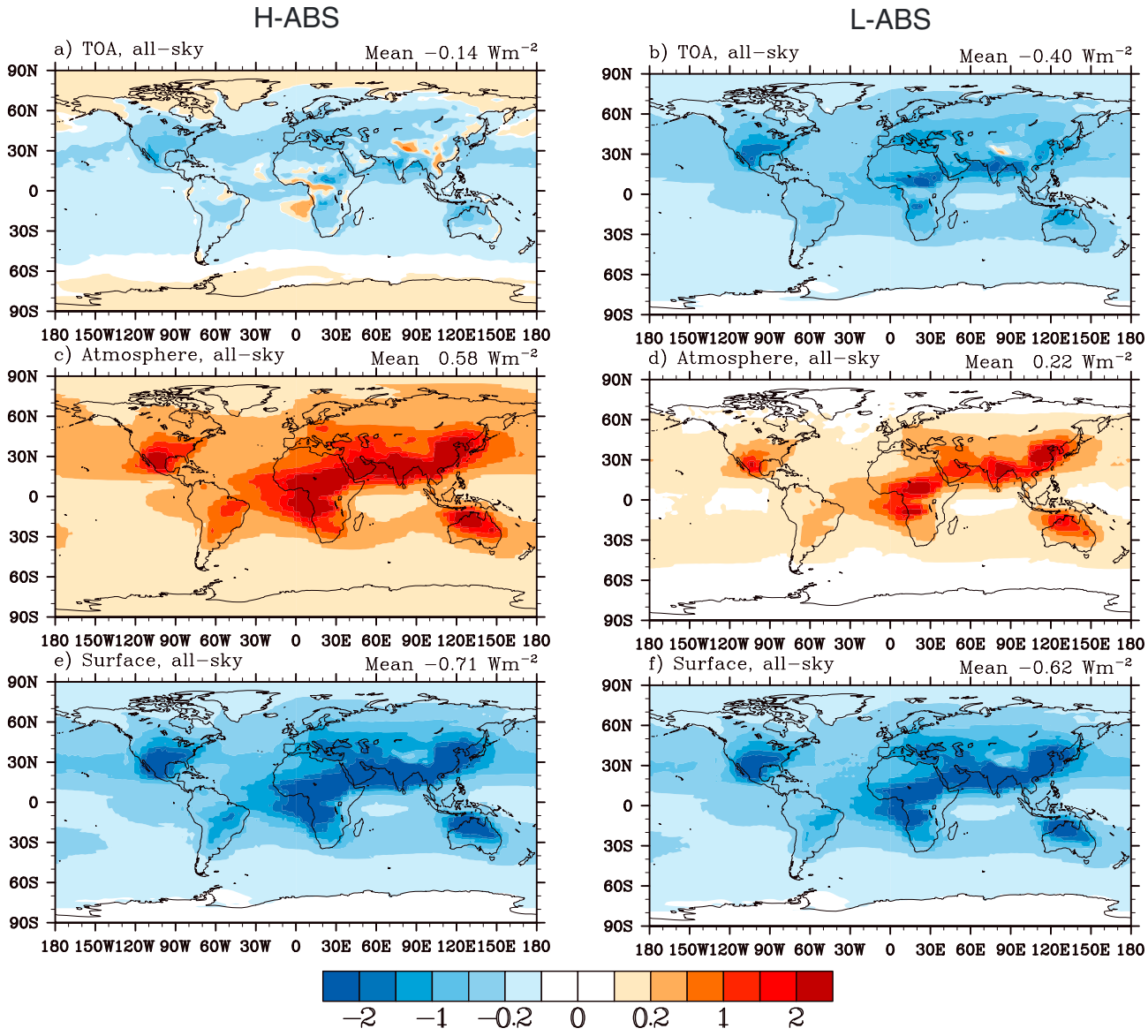

Figure 10. The direct forcing due to the change of the total OA between the PD and PI conditions (a and b) at the TOA, (c and d) in the atmosphere, and (e and f) at the surface for all-sky conditions. Figure 10 (left column) shows the high-absorbing case (H-ABS), while Figure 10 (right column) shows the low-absorbing case (L-ABS).

the reduction of biofuel burning since PI in this region (Figure 4). This reduction is also reflected in the radiative forcing of POA in land snow.

4. Uncertainties in the Radiative Forcing

There are still substantial uncertainties associated with the radiative forcing of OA, mainly resulting from the uncertainty in the mass budget, physical and chemical properties of OA (especially SOA), and their ability to act as cloud condensation nuclei (CCN). The sources, sinks, and chemistry of SOA are uncertain [*Spracklen et al.*, 2011; *Lin et al.*, 2012, 2014] due to the huge number of different atmospheric organic molecules and the complex physical and chemical processes controlling the conversion of gas-phase organics to aerosol [*Hallquist et al.*, 2009]. Our PD global SOA source is larger than that in other models but consistent with the range estimated using top-down methods [*Lin et al.*, 2012, 2014]. In our model, the refractive index and the hygroscopicity are assumed to be constant for all the SOA. Measurements however show that the refractive

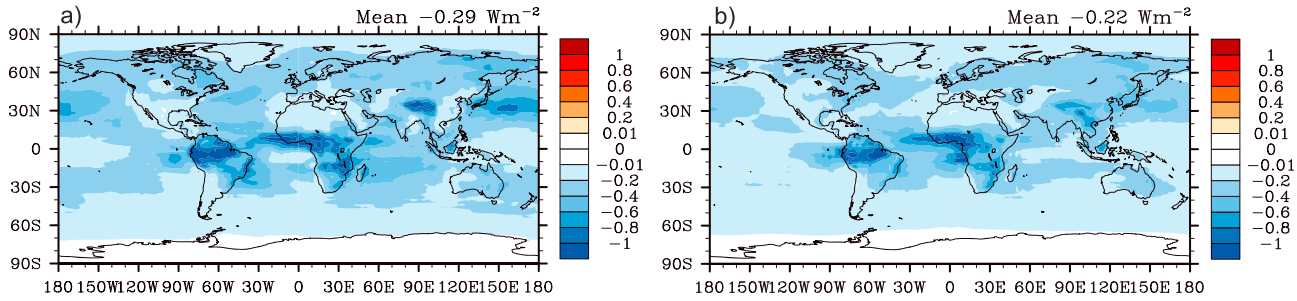

Figure 11. The first indirect aerosol forcing due to the PD-PI difference in SOA. (a) SOA has a lognormal size with a median radius, r_g, equal to 0.08 μm; (b) 43% of the SOA number is assumed to have $r_g = 0.005$ μm and 57% to have $r_g = 0.08$ μm.

index of SOA depends on its source and chemical age in the atmosphere. Moreover, its hygroscopicity has been related to the particle O:C ratio or oxidation stage [*Cappa et al.*, 2011; *Nakayama et al.*, 2013; *Lambe et al.*, 2013]. Thus, a more robust and sophisticated treatment for the optical properties and the hygroscopicity of SOA is needed in the future. In addition, recent laboratory studies and field measurements have shown the importance of organics in the nucleation of new particles [*Metzger et al.*, 2010]. *Metzger et al.* [2010] showed that the rate of nucleation of new particles is proportional to the product of sulfuric acid and condensible organic compounds. *Scott et al.* [2014] used a global aerosol model and showed that including organics in the growth and formation of new particles leads to a much stronger present-day (PD) first indirect effect of biogenic SOA than that when only sulfuric acid contributes. The lack of the explicit use of organics in the aerosol nucleation mechanism in this study therefore may not capture the real aerosol size distribution, although we attempted to account for this in the two size distributions that we assumed. We note that the large present-day indirect effect calculated by *Scott et al.* [2014] (up to -0.77 W m^{-2} for PD when organics are and are not included) may actually decrease the PD-PI forcing as a result of the saturation of indirect effects. The size distribution affects both the direct and indirect effects. Assuming a size distribution with an accumulation mode and a nucleation mode weakens the first indirect forcing of SOA (less negative) by 24% compared to the forcing estimated by assuming that all the SOA particles exist in an accumulation mode. However, assuming a size distribution with an accumulation mode and a nucleation mode results in a stronger direct forcing by 33% (more negative) than the case assuming only an accumulation mode, so the total forcing is quite similar [*Lin*, 2013]. In the model, SOA is assumed to add particle number by converting added SOA mass to number with a prescribed size distribution. This simple increase in particle number is probably not true in reality. Instead, most of SOA may condense or form on preexisting particles to change the size distribution. In the model, we prescribe two different size distributions (i.e., a distribution with only an accumulation mode and a distribution with both an accumulation mode and a nucleation mode) in order to reflect the change of size due to the addition of SOA to preexisting particles to some extent. A more refined approach would need to keep the track of the SOA formed on different particles in the chemical transport model. In addition, the use of an explicit organic nucleation mechanism or the addition of organics to newly formed particles will also affect the aerosol number, which affects the number of particles that can serve as CCN. Finally, it has been shown that fundamental physical climate factors (e.g., cloud cover and relative humidity) have a large impact on aerosol direct radiative forcing [*Ocko et al.*, 2012], which suggests the need to better constrain these factors in future studies.

Table 10. Summary of Estimated Snow/Ice Forcing (W m^{-2}) in Different Simulations Due to the Change of OA

	H-ABS		L-ABS		Other Work	
Case Name	Land Snow	Sea Ice	Land Snow	Sea Ice	Land Snow	Sea Ice
OA	2.5×10^{-3}	5.5×10^{-4}	9.0×10^{-4}	1.6×10^{-4}	-	-
BC	1.2×10^{-2}	9.9×10^{-4}	1.3×10^{-2}	1.0×10^{-3}	3.5×10^{-2} [*Bond et al.*, 2013]	1.1×10^{-2} [*Bond et al.*, 2013]
POA	7.2×10^{-4}	2.0×10^{-4}	6.1×10^{-4}	1.6×10^{-4}	-	-
SOA	1.8×10^{-3}	3.5×10^{-4}	2.8×10^{-4}	-2.8×10^{-6}	-	-

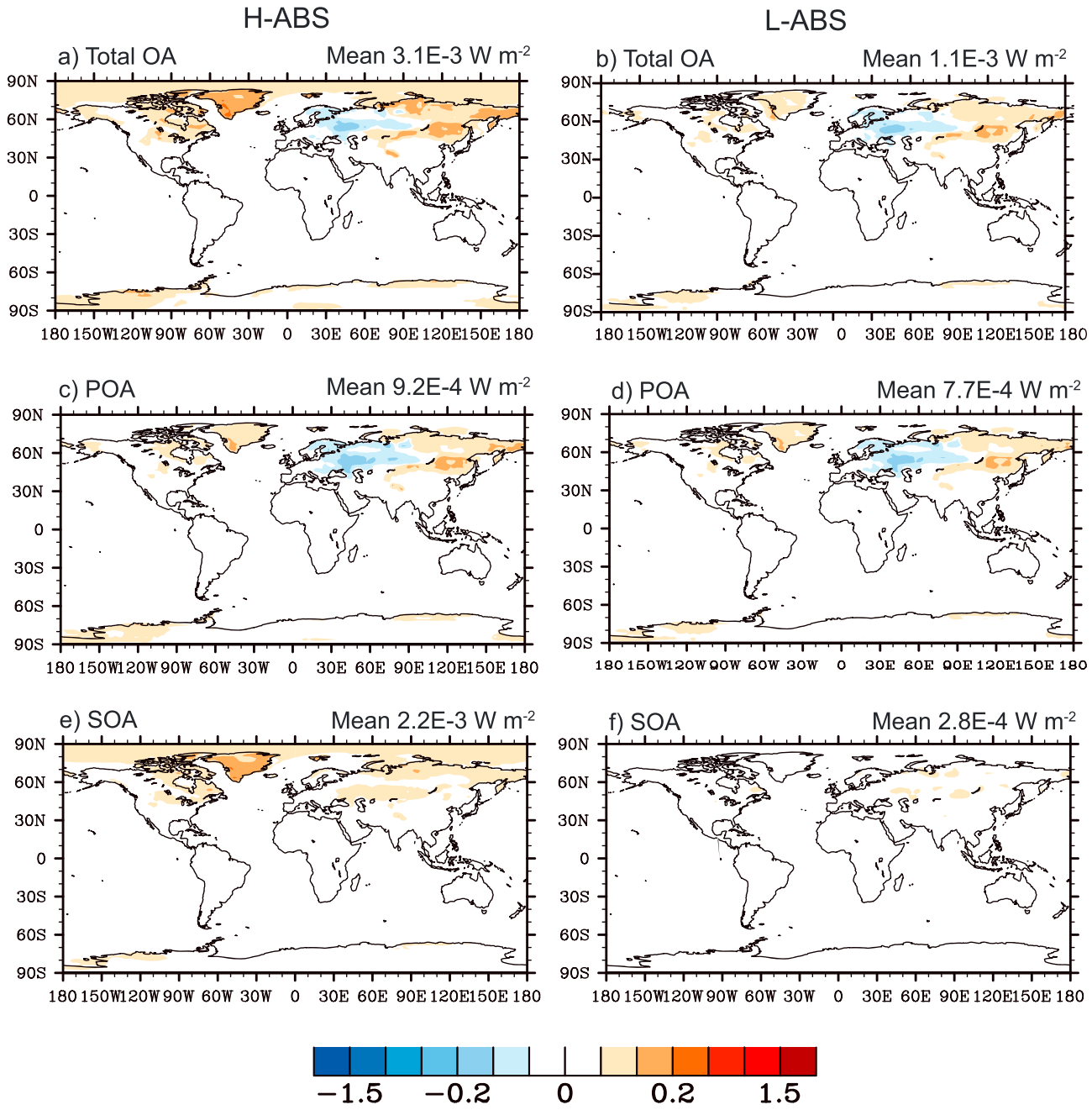

Figure 12. The radiative forcing due to (a and b) the change of OA deposited in land snow and sea ice, (c and d) the change of POA deposited in land snow and sea ice, and (e and f) the change of SOA deposited in land snow and sea ice. Figure 12 (left column) shows the high-absorbing case (H-ABS), while Figure 12 (right column) shows the low-absorbing case (L-ABS).

5. Summary and Discussion

We used a global CTM (IMPACT) to calculate the change in POA and SOA between present-day and preindustrial conditions. We estimate that the increase in anthropogenic emissions increases the POA burden by 0.51 Tg (196%) since PI times. We used an explicit representation of SOA formation mechanisms for the first time and estimated that the total SOA formation rate increased by 29 Tg/yr (94%), while the biogenic SOA formation rate increased by 21.3 Tg/yr (80%) since preindustrial times, mostly as a result of increases in the emissions of NO_x and CO, anthropogenic NMHCs, and CH_4, which affect the formation of SOA precursors

through increasing POA on which SVOCs can condense and through increases in sulfate aerosol on which SOA-forming heterogenous reactions take place.

To account for the light-absorbing part of OA (BrC), we considered two scenarios that apply strongly and weakly absorbing refractive indices and assume different fractions of OA as BrC, thus bracketing the plausible influence of BrC on radiative forcing. The increase of POA since the PI times leads to an all-sky forcing at the TOA varying from -0.06 to $-0.11\,\mathrm{W\,m^{-2}}$ depending on the refractive indices applied to BrC. The PD-PI change in SOA causes a direct radiative forcing of $-0.12\,\mathrm{W\,m^{-2}}$ if 100% of the SOA is assumed to be BrC and its size distribution only includes an accumulation mode, following that of biomass-burning POA. On the other hand, if the BrC fraction and the size of the SOA are assumed to follow those of fossil fuel/biofuel POA, the direct forcing is larger, $-0.31\,\mathrm{W\,m^{-2}}$. The first aerosol indirect forcing of SOA can be as large as $-0.29\,\mathrm{W\,m^{-2}}$ if most SOA particles are in the accumulation mode (r_g near 0.08 μm). If around half of SOA particles are assumed to have a peak in the nucleation mode, the first indirect forcing is $-0.22\,\mathrm{W\,m^{-2}}$. The direct all-sky forcing of the total OA is estimated to range from -0.14 to $-0.40\,\mathrm{W\,m^{-2}}$. Brown carbon causes an atmospheric absorption ranging from +0.22 to $+0.57\,\mathrm{W\,m^{-2}}$.

In comparison with the POA direct forcing estimated by other models, our estimates for the net POA cooling effect are weaker due to the warming effect of BrC. When combining the cooling effect of SOA that is neglected by other models, however, the direct forcing of the total OA is comparable to or even stronger than other model estimates. The absorption by BrC is shown to be important, the magnitude of which in the high-absorbing case could be 57% of the atmospheric absorption caused by BC estimated in the model and over 50% of the atmospheric absorption due to all the anthropogenic aerosols averaged over the AEROCOM phase II models [*Myhre et al.*, 2013].

The PD-PI change in the deposition of OA onto land snow and sea ice is shown, for the first time, to cause a warming of $3.1\times10^{-3}\,\mathrm{W\,m^{-2}}$ in the high-absorbing case and $1.1\times10^{-3}\,\mathrm{W\,m^{-2}}$ in the low-absorbing case. Our high estimate of OA forcing is equal to about 24% of the warming caused by BC in land snow and sea ice estimated in our model and roughly 7% of the best estimate of the warming reported by *Bond et al.* [2013].

One limitation of this work is that the IMPACT model lumps BrC and non-BrC together as one tracer, rather than tracking them separately. This might jeopardize the model's ability to accurately predict the BrC transport and aging in the atmosphere. In the low-absorbing case, we use the local biofuel and residential coal-burning POA emissions as a first-order estimate to scale the BrC content. We assume that there is no BrC when there are no local emissions. This assumption may underestimate the BrC content in the remote regions, where BrC is transported from other regions, rather than locally emitted. We also assume that the fraction of BrC is uniform vertically, based on this scaling of the surface emissions. This approximate treatment does not, of course, fully represent the vertical distribution of BrC. Further work is required to individually track BrC in the model and to incorporate the aging process that might change the solubility of BrC and its light-absorbing ability.

The forcing studied here is limited to the forcing caused by SOA itself. However, the formation of SOA itself changes the concentration of oxidants (e.g., O_3) and SOA precursors in the atmosphere, which could also lead to forcing. Future studies should explore this extra forcing that is indirectly associated with SOA. In addition, we do not account for the forcing of SOA resulting from the change in temperature between the PD and PI or due to the change in CO_2. Biogenic VOC emissions depend on both the atmospheric temperature and the CO_2 concentrations. The change in temperature and CO_2 would affect biogenic VOC emissions, and further affect SOA formation, which would in turn change the temperature. These complex biosphere-SOA-climate interactions cannot be studied using a chemical transport model such as the IMPACT model but rather need to be explored in an earth system model that fully couples an atmospheric general circulation model and a biogenic emission model. Finally, this paper only studies the direct effect and the first indirect effect of OA and does not cover the semidirect effect or the second indirect effect. BrC has been shown to be able to evaporate clouds, which would lead to additional forcings [*Ackerman et al.*, 2000; *Penner et al.*, 2003; *Jacobson*, 2012]. Thus, including the heating-effects of BrC within the atmosphere might decrease clouds and thereby cause even larger net heating.

Acknowledgments
This work was partially funded by the DOE Atmospheric Science Research Program and Earth System Modeling Program through grant DOE FG02 01 ER63248 and the EPA Science to Achieve Results program, grant R-83337701. M.G. Flanner was partially supported by the NSF ARC-1253154.

References

Abdul-Razzak, H., and S. J. Ghan (2000), A parameterization of aerosol activation 2. Multiple aerosol types, *J. Geophys. Res.*, *105*, 6837–6844.
Abdul-Razzak, H., and S. J. Ghan (2002), A parameterization of aerosol activation - 3. Sectional representation, *J. Geophys. Res.*, *107*(D3), 4026, doi:10.1029/2001JD000483.

Ackerman, A. S., O. B. Toon, D. E. Stevens, A. J. Heymsfield, V. Ramanathan, and E. J. Welton (2000), Reduction of tropical cloudiness by soot, *Science*, *288*, 1042–1047.

Andreae, M. O., and A. Gelencsér (2006), Black carbon or brown carbon? The nature of light-absorbing carbonaceous aerosols, *Atmos. Chem. Phys.*, *6*, 3131–3148.

Andres, R. J., and A. D. Kasgnoc (1998), A time-averaged inventory of subaerial volcanic sulfur emissions, *J. Geophys. Res.*, *103*, 25,251–25,261, doi:10.1029/98JD02091.

Arola, A., G. Schuster, and G. Myhre (2011), Inferring absorbing organic carbon content from AERONET data, *Atmos. Chem. Phys.*, *11*, 215–225, doi:10.5194/acp-11-215-2011.

Bahadur, R., P. S. Praveen, Y. Xu, and V. Ramanathan (2012), Solar absorption by elemental and brown carbon determined from spectral observations, *Proc. Natl. Acad. Sci. U. S. A.*, *109*(43), 17,366–17,371.

Bey, I., D. J. Jacob, R. M. Yantosca, J. A. Logan, B. D. Field, A. M. Fiore, Q. B. Li, H. G. Y. Liu, L. J. Mickley, and M. G. Schultz (2001), Global modeling of tropospheric chemistry with assimilated meteorology: Model description and evaluation, *J. Geophys. Res.*, *106*, 23,073–23,095, doi:10.1029/2001JD000807.

Bond, T. C. (2001), Spectral dependence of visible light absorption by carbonaceous particles emitted from coal combustion, *Geophys. Res. Lett.*, *28*, 4075–4078, doi:10.1029/2001GL013652.

Bond, T. C., and R. W. Bergstrom (2006), Light absorption by carbonaceous particles: An investigative review, *Aerosol Sci. Technol.*, *40*(1), 27–67.

Bond, T. C., M. Bussemer, B. Wehner, S. Keller, R. J. Charlson, and J. Heintzenberg (1999), Light Absorption by Primary Particle Emissions from a Lignite Burning Plant, *Environ. Sci. Technol.*, *33*(21), 3887–3891, doi:10.1021/es9810538.

Bond, T. C., et al. (2013), Bounding the role of black carbon in the climate system: A scientific assessment, *J. Geophys. Res. Atmos.*, *118*, 5380–5552, doi:10.1002/jgrd.50171.

Bones, D. L., D. K. Henricksen, S. A. Mang, M. Gonsior, A. P. Bateman, T. B. Nguyen, W. J. Cooper, and S. A. Nizkorodov (2010), Appearance of strong absorbers and fluorophores in limonene-O^3 secondary organic aerosol due to NH 4 + -mediated chemical aging over long time scales, *J. Geophys. Res.*, *115*, D05203, doi:10.1029/2009JD012864.

Cappa, C. D., D. L. Che, S. H. Kessler, J. H. Kroll, and K. R. Wilson (2011), Variations in organic aerosol optical and hygroscopic properties upon heterogeneous OH oxidation, *J. Geophys. Res.*, *116*, D15204, doi:10.1029/2011JD015918.

Chakrabarty, R. K., H. Moosmüller, L. W. A. Chen, K. Lewis, W. P. Arnott, C. Mazzoleni, M. K. Dubey, C. E. Wold, W. M. Hao, and S. M. Kreidenweis (2010), Brown carbon in tar balls from smoldering biomass combustion, *Atmos. Chem. Phys.*, *10*(13), 6363–6370, doi:10.5194/acp-10-6363-2010.

Chang, J. L., and J. E. Thompson (2010), Characterization of colored products formed during irradiation of aqueous solutions containing H2O2 and phenolic compounds, *Atmos. Environ.*, *44*(4), 541–551.

Chen, Y., and T. C. Bond (2010), Light absorption by organic carbon from wood combustion, *Atmos. Chem. Phys.*, *10*, 1773–1787, doi:10.5194/acp-10-1773-2010.

Chung, C. E., V. Ramanathan, and D. Decremer (2012), Observationally constrained estimates of carbonaceous aerosol radiative forcing, *Proc. Natl. Acad. Sci. U.S.A.*, *109*(29), 11,624–11,629.

Chung, S. H., and J. H. Seinfeld (2002), Global distribution and climate forcing of carbonaceous aerosols, *J. Geophys. Res.*, *107*(D19), 4407, doi:10.1029/2001JD001397.

Collins, W. D., P. J. Rasch, B. A. Boville, J. J. Hack, J. R. McCaa, D. L. Williamson, B. P. Briegleb, C. M. Bitz, S. J. Lin, and M. H. Zhang (2006), The formulation and atmospheric simulation of the Community Atmosphere Model version 3 (CAM3), *J. Clim.*, *19*(11), 2144–2161.

Coy, L., and R. Swinbank (1997), Characteristics of stratospheric winds and temperatures produced by data assimilation, *J. Geophys. Res.*, *102*, 25,763–25,781, doi:10.1029/97JD02361.

Deguillaume, L., K. V. Desboeufs, M. Leriche, Y. Long, and N. Chaumerliac (2010), Effect of iron dissolution on cloud chemistry: From laboratory measurements to model results, *Atmos. Pollut. Res.*, *1*(4), 220–228.

Dinar, E., A. Abo Riziq, C. Spindler, C. Erlick, G. Kiss, and Y. Rudich (2007), The complex refractive index of atmospheric and model humic-like substances (HULIS) retrieved by a cavity ring down aerosol spectrometer (CRD-AS), *Faraday Discuss.*, *137*, 279–295, doi:10.1039/b703111d.

Doherty, S. J., S. G. Warren, T. C. Grenfell, A. D. Clarke, and R. E. Brandt (2010), Light-absorbing impurities in Arctic snow, *Atmos. Chem. Phys.*, *10*(23), 11,647–11,680.

Feng, Y., V. Ramanathan, and V. R. Kotamarthi (2013), Brown carbon: A significant atmospheric absorber of solar radiation?, *Atmos. Chem. Phys.*, *13*(17), 8607–8621, doi:10.5194/acp-13-8607-2013.

Flanner, M. G., C. S. Zender, J. T. Randerson, and P. J. Rasch (2007), Present-day climate forcing and response from black carbon in snow, *J. Geophys. Res.*, *112*, D11202, doi:10.1029/2006JD008003.

Flanner, M. G., C. S. Zender, P. G. Hess, N. M. Mahowald, T. H. Painter, V. Ramanathan, and P. J. Rasch (2009), Springtime warming and reduced snow cover from carbonaceous particles, *Atmos. Chem. Phys.*, *9*(7), 2481–2497, doi:10.5194/acp-9-2481-2009.

Forster, P., et al. (2007), Changes in atmospheric constituents and in radiative forcing, in *Climate Change 2007: The Physical Science Basis. Contribution of Working Group I to the Fourth Assessment Report of the Intergovernmental Panel on Climate Change*, edited by S. Solomon et al., 996 pp., Cambridge Univ. Press, Cambridge, U. K., and New York.

Fu, T. M., D. J. Jacob, F. Wittrock, J. P. Burrows, M. Vrekoussis, and D. K. Henze (2008), Global budgets of atmospheric glyoxal and methylglyoxal, and implications for formation of secondary organic aerosols, *J. Geophys. Res.*, *113*, D15303, doi:10.1029/2007JD009505.

Galloway, M. M., P. S. Chhabra, A. W. H. Chan, J. D. Surratt, R. C. Flagan, J. H. Seinfeld, and F. N. Keutsch (2009), Glyoxal uptake on ammonium sulphate seed aerosol: Reaction products and reversibility of uptake under dark and irradiated conditions, *Atmos. Chem. Phys.*, *9*(10), 3331–3345.

Gantt, B., N. Meskhidze, and D. Kamykowski (2009), A new physically-based quantification of marine isoprene and primary organic aerosol emissions, *Atmos. Chem. Phys.*, *9*(14), 4915–4927.

Gondwe, M., M. Krol, W. Gieskes, W. Klaassen, and H. de Baar (2003), The contribution of ocean-leaving DMS to the global atmospheric burdens of DMS, MSA, SO2, and NSS SO4=, *Global Biogeochem. Cycles*, *17*, doi:10.1029/2002GB001937.

Guenther, A., et al. (1995), A global-model of natural volatile organic-compound emissions, *J. Geophys. Res.*, *100*, 8873–8892, doi:10.1029/94JD02950.

Hallquist, M., et al. (2009), The formation, properties and impact of secondary organic aerosol: Current and emerging issues, *Atmos. Chem. Phys.*, *9*(14), 5155–5236.

Hecobian, A., X. Zhang, M. Zheng, and N. Frank (2010), Water-Soluble Organic Aerosol material and the light-absorption characteristics of aqueous extracts measured over the Southeastern United States, *Atmos. Chem. Phys.*, *10*(13), 5965–5977.

Hoffer, A., A. Gelencsér, P. Guyon, and G. Kiss (2006), Optical properties of humic-like substances (HULIS) in biomass-burning aerosols, *Atmos. Chem. Phys.*, *6*(11), 3563–3570.

Holland, M., D. A. Bailey, B. P. Briegleb, B. Light, and E. Hunke (2012), Improved sea ice shortwave radiation physics in CCSM4: The impact of melt ponds and aerosols on Arctic sea ice, *J. Clim.*, *25*, 1413–1430, doi:10.1175/JCLI-D-11-00078.1.

Hoyle, C. R., G. Myhre, T. K. Berntsen, and I. S. A. Isaksen (2009), Anthropogenic influence on SOA and the resulting radiative forcing, *Atmos. Chem. Phys.*, *9*(8), 2715–2728.

Hunke, E. C., and W. H. Lipscomb (2008), CICE: The Los Alamos sea ice model, documentation and software, version 4.0, *Tech. Rep. LA-CC-06-012,* 76 pp., Los Alamos National Laboratory.

IPCC (2013), *Climate Change 2013: The Physical Science Basis. Contribution of Working Group I to the Fifth Assessment Report of the Intergovernmental Panel on Climate Change*, edited by T. F. Stocker et al., 1535 pp., Cambridge Univ. Press, Cambridge, U. K., and New York.

Ito, A. (2011), Mega fire emissions in Siberia: Potential supply of bioavailable iron from forests to the ocean, *Biogeosciences*, *8*, 1679–1697, doi:10.5194/bg-8-1679-2011.

Ito, A., and J. E. Penner (2005), Historical emissions of carbonaceous aerosols from biomass and fossil fuel burning for the period 1870–2000, *Global Biogeochem. Cycles*, *19*, GB2028, doi:10.1029/2004GB002374.

Ito, A., S. Sillman, and J. E. Penner (2007), Effects of additional nonmethane volatile organic compounds, organic nitrates, and direct emissions of oxygenated organic species on global tropospheric chemistry, *J. Geophys. Res.*, *112*, D06309, doi:10.1029/2005JD006556.

Jacobson, M. Z. (1999), Isolating nitrated and aromatic aerosols and nitrated aromatic gases as sources of ultraviolet light absorption, *J. Geophys. Res.*, *104*, 3527–3542, doi:10.1029/1998JD100054.

Jacobson, M. Z. (2001), Global direct radiative forcing due to multicomponent anthropogenic and natural aerosols, *J. Geophys. Res.*, *106*, 1551–1568, doi:10.1029/2000JD900514.

Jacobson, M. Z. (2012), Investigating cloud absorption effects: Global absorption properties of black carbon, tar balls, and soil dust in clouds and aerosols, *J. Geophys. Res.*, *117*, D06205, doi:10.1029/2011JD017218.

Jaoui, M., E. O. Edney, T. E. Kleindienst, M. Lewandowski, J. H. Offenberg, J. D. Surratt, and J. H. Seinfeld (2008), Formation of secondary organic aerosol from irradiated α-pinene/toluene/NOx mixtures and the effect of isoprene and sulfur dioxide, *J. Geophys. Res.*, *113*, D09303, doi:10.1029/2007JD009426.

Jiao, C., et al. (2014), An AeroCom assessment of black carbon in Arctic snow and sea ice, *Atmos. Chem. Phys.*, *14*, 2399–2417, doi:10.5194/acp-14-2399-2014.

Jimenez, J. L., et al. (2009), Evolution of organic aerosols in the atmosphere, *Science*, *326*(5959), 1525–1529, doi:10.1126/science.1180353.

Kanakidou, M., K. Tsigaridis, F. J. Dentener, and P. J. Crutzen (2000), Human-activity-enhanced formation of organic aerosols by biogenic hydrocarbon oxidation, *J. Geophys. Res.*, *105*, 9243–9254, doi:10.1029/1999JD901148.

Kettle, A. J., and M. O. Andreae (2000), Flux of dimethylsulfide from the oceans: A comparison of updated data seas and flux models, *J. Geophys. Res.*, *105*, 26,793–26,808, doi:10.1029/2000JD900252.

Kim, H., B. Barkey, and S. E. Paulson (2012), Real refractive indices and formation yields of secondary organic aerosol generated from photooxidation of Limonene and α-pinene: The effect of the HC/NOx ratio, *J. Phys. Chem. A*, *116*, 6059–6067.

Kirchstetter, T. W., T. Novakov, and P. V. Hobbs (2004), Evidence that the spectral dependence of light absorption by aerosols is affected by organic carbon, *J. Geophys. Res.*, *109*, D21208, doi:10.1029/2004JD004999.

Kirillova, E. N., A. Andersson, J. Han, M. Lee, and Ö. Gustafsson (2014), Sources and light absorption of water-soluble organic carbon aerosols in the outflow from northern China, *Atmos. Chem. Phys.*, *14*, 1413–1422, doi:10.5194/acp-14-1413-2014.

Lack, D. A., J. M. Langridge, R. Bahreini, C. D. Cappa, A. M. Middlebrook, and J. P. Schwarz (2012), Brown carbon and internal mixing in biomass burning particles, *Proc. Natl. Acad. Sci. U.S.A.*, *109*, 14,802–14,807, doi:10.1073/pnas.1206575109.

Lambe, A. T., et al. (2013), Relationship between oxidation level and optical properties of secondary organic aerosol, *Environ. Sci. Technol.*, *47*, 6349–6357, doi:10.1021/es401043j.

Lawrence, D., et al. (2011), Parameterization improvements and functional and structural advances in version 4 of the Community Land Model, *J. Adv. Model. Earth Syst.*, *3*, M03001, doi:10.1029/2011MS000045.

Liao, H., and J. H. Seinfeld (2005), Global impacts of gas-phase chemistry-aerosol interactions on direct radiative forcing by anthropogenic aerosols and ozone, *J. Geophys. Res.*, *110*, D18208, doi:10.1029/2005JD005907.

Lim, H. J., A. G. Carlton, and B. J. Turpin (2005), Isoprene forms secondary organic aerosol through cloud processing: Model simulations, *Environ. Sci. Technol.*, *39*(6), 4441–4446.

Limbeck, A., M. Kulmala, and H. Puxbaum (2003), Secondary organic aerosol formation in the atmosphere via heterogeneous reaction of gaseous isoprene on acidic particles, *Geophys. Res. Lett.*, *30*(19), 1996, doi:10.1029/2003GL017738.

Lin, G. (2013), Global modeling of secondary organic aerosol formation: From atmospheric chemistry to climate, PhD thesis, Univ. of Michigan at Ann Arbor, Ann Arbor.

Lin, G., J. E. Penner, S. Sillman, D. Taraborrelli, and J. Lelieveld (2012), Global modeling of SOA formation from dicarbonyls, epoxides, organic nitrates and peroxides, *Atmos. Chem. Phys.*, *12*, 4743–4774, doi:10.5194/acp-12-4743-2012.

Lin, G., S. Sillman, J. E. Penner, and A. Ito (2014), Global modeling of SOA: The use of different mechanisms for aqueous phase formation, *Atmos. Chem. Phys.*, *14*, 5451–5475, doi:10.5194/acp-14-5451-2014.

Liu, J., et al. (2014), Brown carbon in the continental troposphere, *Geophys. Res. Lett.*, *41*, 2191–2195, doi:10.1002/2013GL058976.

Liu, X. H., J. E. Penner, and M. Herzog (2005), Global modeling of aerosol dynamics: Model description, evaluation, and interactions between sulfate and nonsulfate aerosols, *J. Geophys. Res.*, *110*, D18206, doi:10.1029/2004JD005674.

Liu, X. H., J. Penner, S. Ghan, and M. Wang (2007), Inclusion of ice micro- physics in the NCAR Community Atmospheric Model Version 3 (CAM3), *J. Clim.*, *20*, 4526–4547.

Marley, N. A., et al. (2009), The impact of biogenic carbon sources on aerosol absorption in Mexico City, *Atmos. Chem. Phys.*, *9*(5), 1537–1549, doi:10.5194/acp-9-1537-2009.

Metzger, A., et al. (2010), Evidence for the role of organics in aerosol particle formation under atmospheric conditions, *Proc. Natl. Acad. Sci. U.S.A.*, *107*(15), 6646–6651.

Ming, Y., V. Ramaswamy, P. A. Ginoux, and L. H. Horowitz (2005), Direct radiative forcing of anthropogenic organic aerosol, *J. Geophys. Res.*, *110*, D20208, doi:10.1029/2004JD005573.

Myhre, G., et al. (2013), Radiative forcing of the direct aerosol effect from AeroCom Phase II simulations, *Atmos. Chem. Phys.*, *13*(4), 1853–1877, doi:10.5194/acp-13-1853-2013.

Naik, V., et al. (2013), Preindustrial to present day changes in tropospheric hydroxyl radical and methane lifetime from the Atmospheric Chemistry and Climate Model Intercomparison Project (ACCMIP), *Atmos. Chem. Phys.*, *13*, 5277–5298, doi:10.5194/acp-13-5277-2013.

Nakayama, T., Y. Matsumi, K. Sato, T. Imamura, A. Yamazaki, and A. Uchiyama (2010), Laboratory studies on optical properties of secondary organic aerosols generated during the photooxidation of toluene and the ozonolysis of α-pinene, *J. Geophys. Res.*, *115*, D24204, doi:10.1029/2010JD014387.

Nakayama, T., K. Sato, Y. Matsumi, T. Imamura, A. Yamazaki, and A. Uchiyama (2012), Wavelength dependence of refractive index of secondary organic aerosols generated during the ozonolysis and photooxidation of α-pinene, SOLA, *8*, 119–123, doi:10.2151/sola.2012-030.

Nakayama, T., K. Sato, Y. Matsumi, T. Imamura, A. Yamazaki, and A. Uchiyama (2013), Wavelength and NO_x dependent complex refractive index of SOAs generated from the photooxidation of toluene, *Atmos. Chem. Phys.*, *13*(2), 531–545, doi:10.5194/acp-13-531-2013.
Ocko, I. B., V. Ramaswamy, and P. Ginoux (2012), Sensitivity of scattering and absorbing aerosol direct radiative forcing to physical climate factors, *J. Geophys. Res.*, *117*, D20203, doi:10.1029/2012JD018019.
O'Dowd, C. D., B. Langmann, S. Varghese, C. Scannell, D. Ceburnis, and M. C. Facchini (2008), A combined organic inorganic sea-spray source function, *Geophys. Res. Lett.*, *35*, L01801, doi:10.1029/2007GL030331.
Oleson, K. W., et al. (2010), Technical description of version 4.0 of the Community Land Model, *NCAR Tech. Note NCAR/TN-478+STR*, 257 pp.
Paulot, F., J. D. Crounse, H. G. Kjaergaard, A. Kurten, J. M. St Clair, J. H. Seinfeld, and P. O. Wennberg (2009), Unexpected epoxide formation in the gas-phase photooxidation of isoprene, *Science*, *325*(5941), 730–733.
Peeters, J., T. L. Nguyen, and L. Vereecken (2009), HOx radical regeneration in the oxidation of isoprene, *Phys. Chem. Chem. Phys.*, *11*(28), 5935–5939.
Penner, J. E., S. Y. Zhang, and C. C. Chuang (2003), Soot and smoke aerosol may not warm climate, *J. Geophys. Res.*, *108*(D21), 4657, doi:10.1029/2003JD003409.
Penner, J. E., L. Xu, and M. Wang (2011a), Satellite methods underestimate indirect climate forcing by aerosols, *Proc. Natl. Acad. Sci. U.S.A.*, *108*, 13,404–13,408.
Penner, J. E., C. Zhou, L. Xu, and M. Wang (2011b), Reply to Quaas et al.: Can satellites be used to estimate indirect climate forcing by aerosols?, *Proc. Natl. Acad. Sci. U.S.A.*, *108*, E1100–E1101, doi:10.1073/pnas.1116135108.
Prather, M., C. Holmes, and J. Hsu (2012), Reactive greenhouse gas scenarios: Systematic exploration of uncertainties and the role of atmospheric chemistry, *Geophys. Res. Lett.*, *39*, L09803, doi:10.1029/2012GL051440.
Rotstayn, L. D., and Y. G. Liu (2003), Sensitivity of the first indirect aerosol effect to an increase of cloud droplet spectral dispersion with droplet number concentration, *J. Clim.*, *16*(21), 3476–3481.
Saleh, R., C. J. Hennigan, G. R. McMeeking, W. K. Chuang, E. S. Robinson, H. Coe, N. M. Donahue, and A. L. Robinson (2013), Absorptivity of brown carbon in fresh and photo-chemically aged biomass-burning emissions, *Atmos. Chem. Phys.*, *13*(15), 7683–7693, doi:10.5194/acp-13-7683-2013.
Sareen, N., S. G. Moussa, and V. F. McNeill (2013), Photochemical aging of light-absorbing secondary organic aerosol material, *J. Phys. Chem. A*, *117*(14), 2987–2996.
Schulz, M., et al. (2006), Radiative forcing by aerosols as derived from the AeroCom present-day and pre-industrial simulations, *Atmos. Chem. Phys.*, *6*(12), 5225–5246, doi:10.5194/acp-6-5225-2006.
Scott, C. E., et al. (2014), The direct and indirect radiative effects of biogenic secondary organic aerosol, *Atmos. Chem. Phys.*, *14*, 447–470, doi:10.5194/acp-14-447-2014.
Shapiro, E. L., J. Szprengiel, N. Sareen, C. N. Jen, M. R. Giordano, and V. F. McNeill (2009), Light-absorbing secondary organic material formed by glyoxal in aqueous aerosol mimics, *Atmos. Chem. Phys.*, *9*(7), 2289–2300, doi:10.5194/acp-9-2289-2009.
Smith, S. J., H. Pitcher, and T. M. L. Wigley (2001), Global and regional anthropogenic sulfur dioxide emissions, *Global Planet. Change*, *29*(1–2), 99–119, doi:10.1016/S0921-8181(00)00057-6.
Spracklen, D. V., et al. (2011), Aerosol mass spectrometer constraint on the global secondary organic aerosol budget, *Atmos. Chem. Phys.*, *11*(23), 12,109–12,136.
Takemura, T., T. Nozawa, S. Emori, T. Y. Nakajima, and T. Nakajima (2005), Simulation of climate response to aerosol direct and indirect effects with aerosol transport-radiation model, *J. Geophys. Res.*, *110*, D02202, doi:10.1029/2004JD005029.
Trainic, M., A. Abo Riziq, A. Lavi, J. M. Flores, and Y. Rudich (2011), The optical, physical and chemical properties of the products of glyoxal uptake on ammonium sulfate seed aerosols, *Atmos. Chem. Phys.*, *11*(18), 9697–9707, doi:10.5194/acp-11-9697-2011.
Tsigaridis, K., M. Krol, F. J. Dentener, Y. Balkanski, J. Lathiere, S. Metzger, D. A. Hauglustaine, and M. Kanakidou (2006), Change in global aerosol composition since preindustrial times, *Atmos. Chem. Phys.*, *6*, 5143–5162.
Turpin, B. J., and H. J. Lim (2001), Species contributions to PM2. 5 mass concentrations: Revisiting common assumptions for estimating organic mass, *Aerosol Sci. Technol.*, *35*, 602–610.
Updyke, K. M., T. B. Nguyen, and S. A. Nizkorodov (2012), Formation of brown carbon via reactions of ammonia with secondary organic aerosols from biogenic and anthropogenic precursors, *Atmos. Environ.*, *63*, 22–31, doi:10.1016/j.atmosenv.2012.09.012.
van Aardenne, J. A., F. J. Dentener, J. G. J. Olivier, C. G. M. Klein Goldewijk, and J. Lelieveld (2001), A 1×1 degree resolution dataset of historical anthropogenic trace gas emissions for the period 1890–1990, *Global Biogeochem. Cycles*, *15*, 909–928, doi:10.1029/2000GB001265.
Wang, M. H., and J. E. Penner (2009), Aerosol indirect forcing in a global model with particle nucleation, *Atmos. Chem. Phys.*, *9*(1), 239–260.
Wang, M. H., J. E. Penner, and X. H. Liu (2009), Coupled IMPACT aerosol and NCAR CAM3 model: Evaluation of predicted aerosol number and size distribution, *J. Geophys. Res.*, *114*, D06302, doi:10.1029/2008JD010459.
Wang, Y. H., D. J. Jacob, and J. A. Logan (1998), Global simulation of tropospheric O-3-NOx-hydrocarbon chemistry 1. Model formulation, *J. Geophys. Res.*, *103*, 10,713–10,725, doi:10.1029/98JD00158.
Waxman, E. M., K. Dzepina, B. Ervens, J. Lee-Taylor, B. Aumont, J. L. Jimenez, S. Madronich, and R. Volkamer (2013), Secondary organic aerosol formation from semi- and intermediate-volatility organic compounds and glyoxal: Relevance of O/C as a tracer for aqueous multiphase chemistry, *Geophys. Res. Lett.*, *40*, 978–982, doi:10.1002/grl.50203.
Woo, J. L., D. D. Kim, A. N. Schwier, R. Li, and V. F. McNeill (2013), Aqueous aerosol SOA formation: Impact on aerosol physical properties, *Faraday Discuss.*, *165*, 357–367.
Yang, M., S. G. Howell, and J. Zhuang (2009), Attribution of aerosol light absorption to black carbon, brown carbon, and dust in China–interpretations of atmospheric measurements during EAST-AIRE, *Atmos. Chem. Phys.*, *9*, 2035–2050, doi:10.5194/acp-9-2035-2009.
Young, P. J., et al. (2013), Pre-industrial to end 21st century projections of tropospheric ozone from the Atmospheric Chemistry and Climate Model Intercomparison Project (ACCMIP), *Atmos. Chem. Phys.*, *13*(4), 2063–2090, doi:10.5194/acp-13-2063-2013.
Yun, Y., J. E. Penner, and O. Popovicheva (2013), The effects of hygroscopicity on ice nucleation of fossil fuel combustion aerosols in mixed-phase clouds, *Atmos. Chem. Phys.*, *13*, 4339–4348, doi:10.5194/acp-13-4339-2013.
Zhang, Q., et al. (2007), Ubiquity and dominance of oxygenated species in organic aerosols in anthropogenically-influenced Northern Hemisphere midlatitudes, *Geophys. Res. Lett.*, *34*, L13801, doi:10.1029/2007GL029979.
Zhang, S., J. E. Penner, and O. Torres (2005), Inverse modeling of biomass burning emissions using Total Ozone Mapping Spectrometer aerosol index for 1997, *J. Geophys. Res.*, *110*, D21306, doi:10.1029/2004JD005738.
Zhang, X., Y.-H. Lin, J. D. Surratt, P. Zotter, A. S. H. Prévôt, and R. J. Weber (2011), Light-absorbing soluble organic aerosol in Los Angeles and Atlanta: A contrast in secondary organic aerosol, *Geophys. Res. Lett.*, *38*, L21810, doi:10.1029/2011GL049385.
Zhang, X., Y.-H. Lin, J. D. Surratt, and R. J. Weber (2013), Sources, composition and absorption angström exponent of light-absorbing organic components in aerosol extracts from the Los Angeles Basin, *Environ. Sci. Technol.*, *47*(8), 3685–3693.
Zhong, M., and M. Jang (2011), Light absorption coefficient measurement of SOA using a UV–Visible spectrometer connected with an integrating sphere, *Atmos. Environ.*, *45*, 4263–4271.